Differential exhumation of the Eastern Cordillera in the Central Andes: Evidence for south-verging backthrusting (Abancay Deflection, Peru)

Benjamin Gérard[1], Xavier Robert[1], Laurence Audin[1], Pierre G. Valla[1,2], Matthias Bernet[1], Cécile Gautheron[3]

[1]Univ. Grenoble Alpes, Univ. Savoie Mont Blanc, CNRS, IRD, IFSTTAR, ISTerre, 38000 Grenoble, France

[2]Institut of Geological Sciences, University of Bern, Baltzerstrasse 3, 3012 Bern, Switzerland

[3] Université Paris-Saclay, CNRS, GEOPS, 91405, Orsay, France

Corresponding author: Benjamin Gérard (benjamin.gerard.alpes@gmail.com)

Key Points:

- Thermochronological data quantifying the tectonic history of the undocumented northern edge of the Peruvian Altiplano (Abancay Deflection)
- 3-D Thermo-kinematic models unravel the evolution of the Eastern Cordillera & the Altiplano
- Steady and uniform exhumation between 40 and 5 Ma, followed by tectonically-driven tilting of the Eastern Cordillera

Abstract

Located at the northern tip of the Altiplano, the Abancay Deflection marks abruptly the latitudinal segmentation of the Central Andes spreading over the Altiplano to the south and the Eastern Cordillera northward. The striking contrast in terms of morphology between the low-relief Altiplano and the high-jagged Eastern Cordillera makes this area a privileged place to determine spatio-temporal variations in surface and/or rock uplift and discuss the latest phase of the formation of the Central Andes. Here, we aim to quantify exhumation and uplift patterns in the Abancay Deflection since 40 Ma, and present new apatite (U-Th)/He and fission-track data from five altitudinal profiles and additional individual samples. Age-Elevation relationships and thermal modeling both evidence that the Abancay Deflection experienced a moderate, spatially-uniform and steady exhumation at 0.2±0.1 km/m.y. between 40 Ma and ~5 Ma implying common large-scale exhumation mechanisms. From ~5 Ma, while the northern part of the Eastern Cordillera and the Altiplano registered similar ongoing slow exhumation, the southern part of the Eastern Cordillera experienced one order-of-magnitude of exhumation acceleration (1.2±0.4 km/m.y). This differential exhumation since ~5 Ma implies active tectonics, river capture and incision affecting the southern Eastern Cordillera. 3D thermo-kinematic modeling favors a tectonic decoupling between the Altiplano and the Eastern Cordillera through backthrusting activity of the Apurimac fault. We speculate that the Abancay Deflection, with its "bulls-eye" structure and significant exhumation rate since 5 Ma, may represent an Andean proto-syntaxis, similar to the syntaxes described in the Himalaya or Alaska.

Keywords: Central Andes, Abancay Deflection, Thermochronology, Differential exhumation, Tectonic decoupling, Apurimac fault system

1 Introduction

The Central Andes contain the second-highest and widest plateau on Earth: the Altiplano. Andean topography building started during the Cretaceous (~120-110 Ma; Jaillard & Soler, 1996). Tectonic, climatic and erosional interactions affecting the Altiplano and its eastward border, the Eastern Cordillera (Figure 1), have been extensively studied in the southern Central Andes (Bolivia, Argentina; Strecker et al., 2007). The northern edge of the Altiplano, namely the Abancay Deflection (southern Peru; Marocco, 1971; Dalmayrac et al., 1980; Gérard et al., submitted), however, has been poorly documented, although its relief and structural organization reveals spectacular specificities with deflected drainage basins and rivers, and deeply-incised landforms. The Abancay Deflection occupies a part of the Altiplano to the south and the Eastern Cordillera northward (Figures 1 & 2), and is limited to the north by the Subandes. Morphologically, the Altiplano and the Eastern Cordillera acquired their respective modern mean elevation of ~4 km and ~4.5 km before 5 Ma (Sundell et al., 2019).

Mechanisms for exhumation of the Bolivian and southern Peru Eastern Cordillera are debated and imply either east-verging thrusting along a ramp connected to the Subandean zone (Gotberg et al., 2010; Rak et al., 2017), or reactivation of inherited faults as west-verging backthrusts (Perez et al., 2016), both with subsequent erosion of the built topography. In Bolivia, the Eastern Cordillera experienced exhumation between 50 and 15 Ma with transfer of tectonic deformation to the Subandean zone at ~15 Ma (Barnes et al., 2012). From thermochronological records, the northern Altiplano has been suggested to experience a steady exhumation of ~0.2 km/m.y. between ~40 and ~15 Ma (Ruiz et al., 2009). The limited records before 38 Ma and after 14 Ma for this area, however, prevents from deciphering and/or speculating between different surface-uplift scenarios such as slow and continuous surface uplift associated with (lower) crustal deformation since 40 Ma (Barnes & Ehlers,

2009; Husson & Sempere, 2003; Ouimet & Cook, 2010), versus potential surface-uplift acceleration during the Miocene triggered by lithospheric delamination event(s) (Garzione et al., 2017). The high-relief Eastern Cordillera seems to register a more recent and complex exhumation history (< 5 Ma) with both incision and regressive erosion (Lease and Ehlers, 2013; Gérard et al. submitted).

Regarding the climate imprint over the Eastern Cordillera, major canyon carving is supposedly related to Pliocene global climate cooling (Lease & Ehlers, 2013). Nonetheless, increased orographic precipitation in such a rising orogen (Insel et al., 2010), could explain also canyon incision events earlier than the Pliocene (Poulsen et al., 2010). Even though the timing of surface uplift and mechanisms of exhumation are debated, there is a clear contrast and decoupling in terms of vertical motion between the Altiplano, the Eastern Cordillera and the Subandes. Our aim is to provide further quantitative constraints to unravel the mechanisms responsible for the Abancay Deflection exhumation and uplift since 40 Ma.

The deeply-incised Abancay Deflection is the ideal target to unravel the long-term evolution of the northern edge of the Altiplano (Figure 1). Here we present new apatite (U-Th)/He (AHe) and fission-track (AFT) data, targeting Permo-Triassic (Mišković et al., 2009) and Paleogene (Carlier et al., 1996; Mamani et al., 2010) plutonic bedrocks along high-relief valleys. We have interpreted these thermochronological data using Age-Elevation Relationships (AER; Glotzbach et al., 2011), thermal (2D; QTQt; Gallagher, 2012) and thermo-kinematic (3D; Pecube; Braun, 2003; Braun et al., 2012) modeling to determine the late-Eocene to modern exhumation history of the Abancay Deflection and discuss potential exhumation mechanisms.

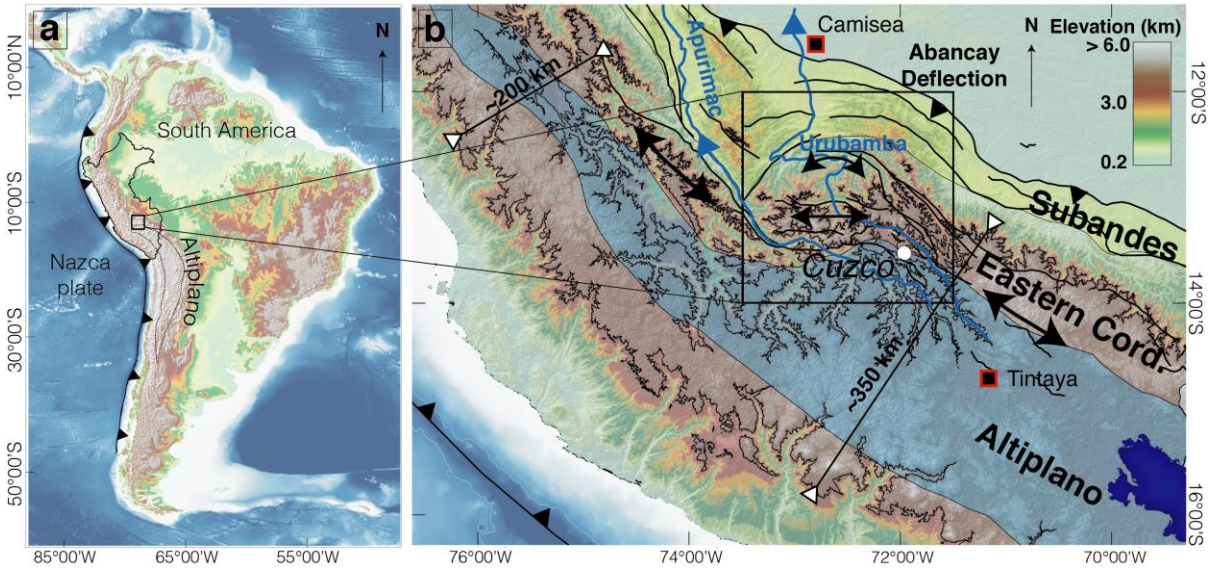

Figure 1. Abancay Deflection location. a) Location within South America of the study area at the northern tip of the Altiplano in Peru. b) Zoom-in on the Abancay Deflection area (black square in panel a). Double black arrows highlight the topography elongation axis. Note the pronounced incision within the study area through the iso-elevation line (black) at 3.8 km elevation via the Urubamba and Apurimac rivers (blue) canyons. Black thin lines framed by white triangles highlight the latitudinal range width variation with the Abancay Deflection as the transition zone between the northern narrow Peruvian Andes and the southern wide Bolivian Orocline. Black squares with red borders are the places where thermal parameters were measured.

2 Geological setting

The Abancay Deflection occupies the morpho-tectonic regions of the Altiplano to the south and the Eastern Cordillera to the north, separated by the crustal-scale Apurimac fault system (Figure 2). This fault system seems to affect the study area since at least the Permian (by a transform fault in an extensional context; Sempere et al., 2002). Eocene plutons (50-30 Ma; Mamani et al., 2010) emplaced into Meso-Cenozoic sediments (Carlier et al., 1996) crop out in the Altiplano whereas Permo-Triassic batholiths are dominant in the Eastern Cordillera and intrude into Paleozoic rocks (Figure 2; Mišković et al., 2009). Thermal perturbation linked to magmatic arc activity ceased after ~30 Ma and the ultimate local volcanic events (from 7 to 0.5 Ma; Bonhomme et al., 1988) focused along the Apurimac fault system. Inherited deflected faults and arched-captured rivers characterize the Abancay Deflection on the northern edge of the Altiplano that records high-magnitude counterclockwise tectonic rotation since 40 Ma (Roperch et al., 2006) in a Bolivian Orocline bending context (Müller et al., 2002).

The Subandean zone and the Altiplano are documented as tectonically active respectively in shortening and extensional context (Figure 3) since ~14 Ma in the Subandes (Espurt et al., 2011; Gautheron et al., 2013) and since ~5 Ma in the Altiplano (Cabrera et al., 1991). In between, the Eastern Cordillera limited southward by the Apurimac fault system presents nowadays a non-negligible low-magnitude crustal seismicity (Figure 3a), however, too low to determine a tectonic behavior (Figure 3b). Preliminary thermochronological investigation into the core of the Eastern Cordillera (Machu Picchu), nonetheless, favors a post ~4 Ma acceleration of incision-driven exhumation but this inference is restricted to the local area of Machu Picchu and cannot be extended yet for the entire Abancay Deflection (Gérard et al. Submitted). Also, this previous study can neither evidence nor discard potential tectonic-driven exhumation. The observed seismicity for the Apurimac fault system area

could be linked and/or connected with either Subandean flat-ramp thrust systems or undocumented active internal backthrusts, or even normal faulting as in the Altiplano. Though, potential tectonic drivers responsible for the building of the Abancay Deflection and particularly for the Eastern Cordillera part remain unknown. Quantitative thermochronology and modeling represent the ideal tools to explore exhumation pattern for the whole area addressing exhumation mechanisms.

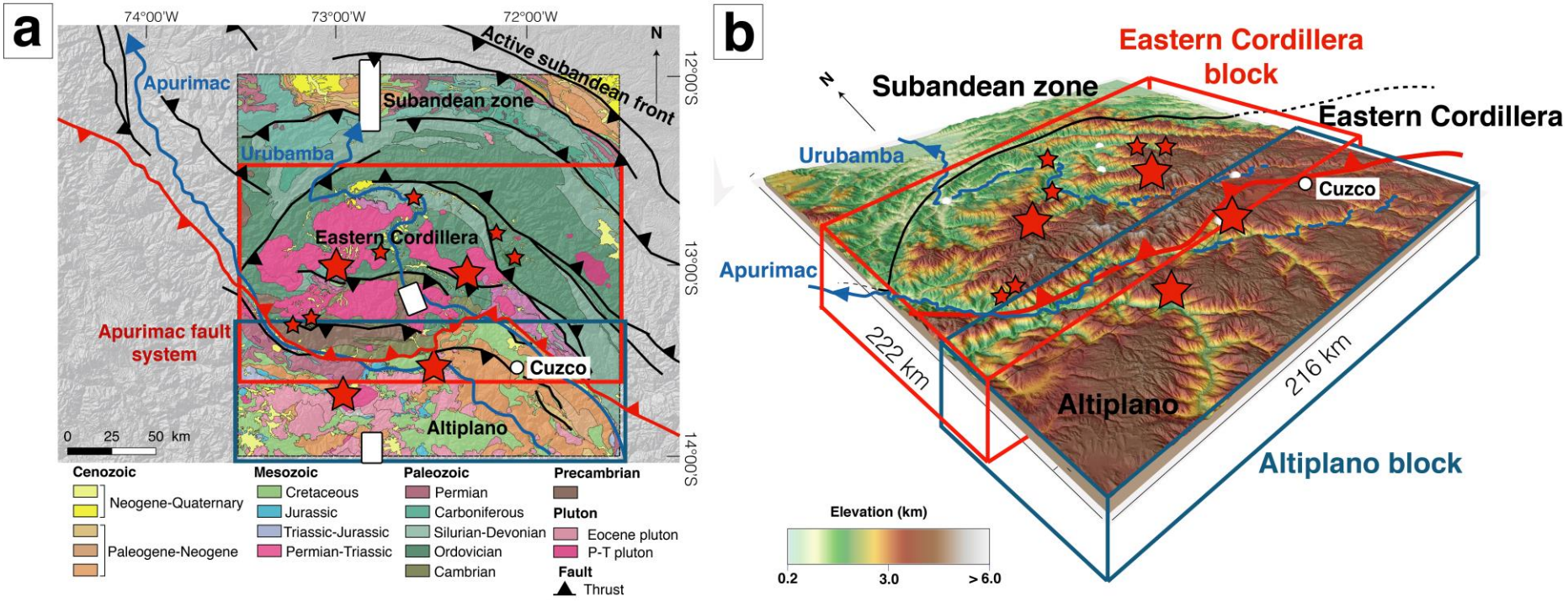

Figure 2. Geology and morphology of the Abancay Deflection. a) Geological map of the study area. The crustal scale Apurimac fault system marks the tectonic limit between the Altiplano and the Eastern Cordillera. (INGEMMET geological map database - 1:100,000). White rectangles refer to previous thermochronological studies; references are provided in the method and results sections. b) 3D DEM of the Abancay Deflection. For both panels, red stars are the thermochronological sample location (vertical profiles and individual data; this study). 2D colored rectangles (a) and corresponding 3D views (b) are crustal block locations processed with 3D thermo-kinematics modeling using Pecube for the Altiplano (blue) and the Eastern Cordillera (red) blocks.

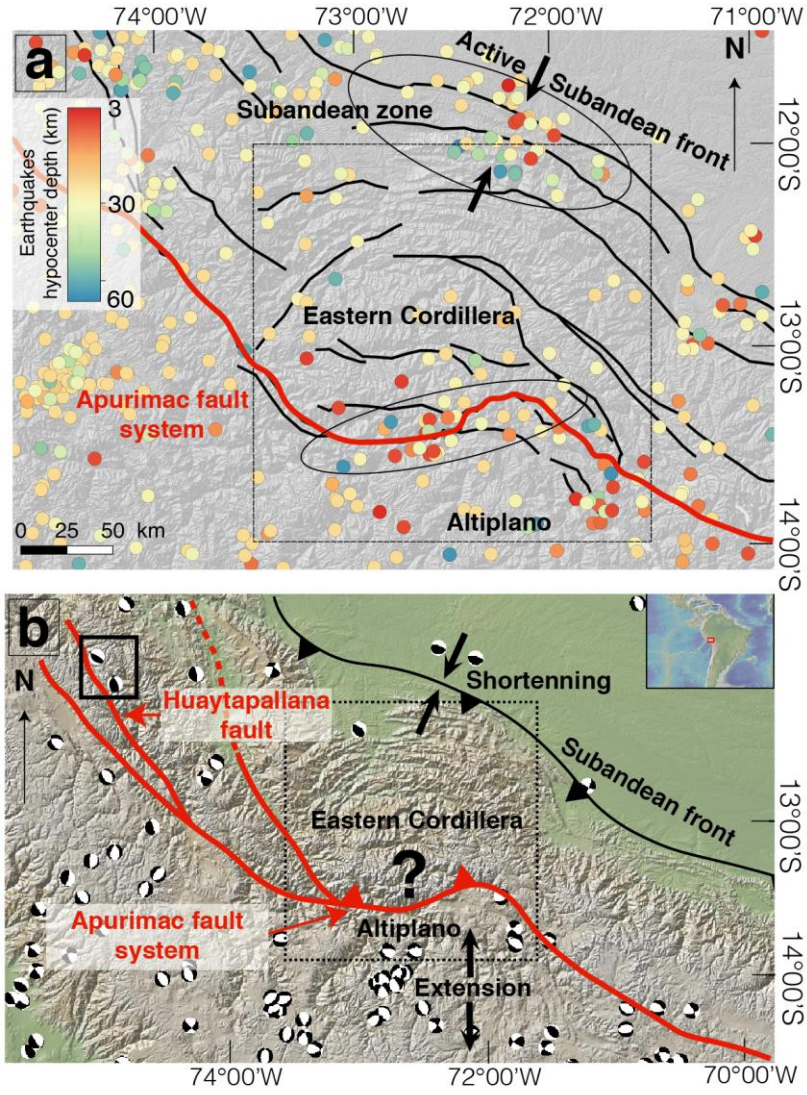

Figure 3. Crustal seismic map of the Abancay Deflection (Dashed squares; hypocenters < 60 km; Mw > 2). a) Mapped earthquakes come from the USGS, IGP and ISC databases. Regions included into black ellipses emphasize positive anomalous cluster of seismicity. Black lines represent the major thrusts of the studied area. b) Moment tensors (CMT) for earthquakes (1969-2019) for the Abancay Deflection region (Dziewonski et al., 1981; Ekström et al., 2012). Focal mechanisms (transpressional) for the two 1969 Huaytapallana events are framed by the black rectangle (Dorbath et al., 1990; Suarez et al., 1983). There are no CMT data for Mw < 5.5 earthquakes. Tectonic shortening characterizes the Subandean front whereas extensional mechanisms affect the Altiplano.

3 Methods

AHe and AFT thermochronology are based on He and fission track production during alpha decay of U, Th and Sm and fission decay of U respectively with associated He and fission tracks accumulation within apatite crystals. Using a rate of He diffusion rate out of the crystals or fission track annealing with temperature, those methods can be used to record the thermal evolution of the upper crust, given their thermal sensitivity ranges spanning from ~80-40°C (Ault et al., 2019) and ~75-125°C (Reiners & Brandon, 2006) respectively for active mountain ranges, depending on cooling rate and/or holding time within the respective partial retention/annealing zones. Thus, low-temperature thermochronology records the thermal evolution of the upper crust (< 5 km) and is a key to decipher between different exhumation mechanisms through time-evolving rock uplift and landscape evolution (Ault et al., 2019; Reiners & Shuster, 2009). Quantitative interpretation with three different types of models (*i.e.* geometric, thermal and thermo-kinematic, sections 3.2-3.4) with different degrees of complexity makes it possible to test model robustness and propose highly consistent scenarios for the exhumation of the Abancay Deflection.

3.1 Low-temperature thermochronological data

We collected 33 samples from magmatic bedrock of five high-altitude profiles (Ocobamba, Lucma, Incahuasi, Abancay and Limatambo) and 4 individual samples collected across the Abancay Deflection to get an optimal coverage of the study area (Figures 2 & 4; Table 1). Granitic samples were crushed and sieved at the Géode laboratory (Lyon, France) to extract the 100-160 µm fractions. Apatite crystals were concentrated using standard magnetic and heavy-liquid separation techniques at the GeoThermoChronology (GTC) platform within the ISTerre laboratory (Université Grenoble Alpes, France).

For AHe dating single euhedral apatite crystals were carefully selected under a binocular microscope to identify minerals without fractures and/or inclusions that would skew the AHe age (diffusion artifacts and/or additional ^{4}He sources; Farley, 2002). We determined the individual grain geometry and calculated the alpha-ejection correction factor using the Qt_FT program (Gautheron and Tassan-Got, 2010; Ketcham et al., 2011). Individual apatites were encapsulated in platinum tubes allowing apatite heating and manipulation. Each apatite in its platinum tube was then heated under ultra-vacuum conditions at high temperature (1050±50°C using an infrared diode laser) twice for 5 min at GEOPS laboratory (Université Paris Saclay, France). The ^{4}He gas was mixed with a known amount of ^{3}He, purified and the gas was analyzed using a Prisma Quadrupole. The ^{4}He content was determined by isotopic dilution. Subsequently, apatite crystals were dissolved in 100 µl of HNO_3 5N solution containing known amount of ^{235}U, ^{230}Th, ^{149}Sm and ^{42}Ca. The solution was heated at 70°C during 3 h and after a cooling time, 900 µl of distilled water was added. The final solution was analyzed using an ELEMENT XR ICP-MS and the ^{238}U, ^{230}Th and ^{147}Sm concentrations and apatite weight (using the Ca content) were determined following the methodology proposed by Evans et al. (2005). Durango apatite crystals were also analyzed during the same period to ensure the data quality. The one-sigma error on each AHe age amounts to 8%, reflecting the analytical error and the uncertainty on the FT ejection factor correction. More details about the analytical procedure can be found in Recanati et al. (2017).

For AFT dating at the GTC laboratory (ISTerre, Grenoble, France), apatites were mounted in epoxy resin, polished, and etched for 20 s at 21°C using a 5.5 M HNO_3 solution to reveal spontaneous fission tracks. Using the external detector method, all samples were irradiated together with age standards at IRMM540R dosimeter glasses at the FRM II reactor (Munich, Germany). Tracks were counted and horizontally confined track lengths were

214 measured at ISTerre. We used the BINOMFIT program (Ehlers et al., 2005) to calculate the
215 AFT central ages.
216
217 **3.2 Age-Elevation Relationships (AER)**
218 For AER modeling, single- or multi-tier age-elevation relationships (AER) to the AFT
219 and AHe data from altitudinal profile data were fit using a Bayesian approach to obtain a
220 first-order estimate of apparent exhumation rates and evidence potential break-in-slope
221 through time by minimization of the Bayesian Information Criterion (BIC; Glotzbach et al.,
222 2011; Schwarz, 1978). This process gives first-order constraints regarding exhumation rates
223 and potential exhumation changes through time for each vertical profile. These apparent
224 exhumation rates are, nonetheless, free from any consideration regarding the inter-sample
225 AHe/AFT kinetic variability, the thermal crustal regime, the relief evolution and the isostasy
226 assuming a quasi-vertical profile (Stüwe et al., 1994). These modeling biases will be taken
227 into account with 2D thermal and 3D thermo-kinematic modeling described hereafter.
228
229 **3.3 Time-temperature modeling (QTQt)**
230 Time-temperature modeling with QTQt (Bayesian transdimensional and MCMC
231 sampling; Gallagher, 2012) gives strong constrains regarding thermal histories for individual
232 samples, with the possibility to combine and process multi-samples from high-altitudinal
233 profiles. We processed 300,000 iterations for both individual sample and vertical profiles
234 exploring T-t paths with their respective likelihood allowing extracting best-fitting thermal
235 histories. We used the implemented annealing model of Ketcham et al. (2007) and the
236 radiation damage model of Gautheron et al. (2009) for AFT and AHe data respectively. We
237 allowed the geothermal gradient to vary over time for values spreading over 10 and 40°C/km
238 commonly associated for the non-volcanic Central Andes (Barnes et al., 2008). The timespan

239 explored starts twice as the older thermochronological age for each profile to eliminate any
240 potential temporal bias.

241 Assessing the geothermal gradient is a crucial point for exhumation rate computation,
242 and the Abancay Deflection is totally devoid of direct measurements. We computed a
243 geothermal gradient according to the nearest thermal parameter measurements and/or
244 accepted values for these parameters. According to heat flow and thermal conductivity
245 measurements in the Tintaya mine (Figure 1b; Henry & Pollack, 1988), crustal average heat
246 production (~0.9 $\mu W/m^3$; Springer, 1999), thermal diffusivity for a granitic bedrock (~40
247 $km^2/m.y.$; Arndt et al., 1997; Whittington et al., 2009) and a ~25°C surface temperature
248 (Gonfiantini et al., 2001) we obtained a geothermal gradient of 18±4°C/km (Text S1). This
249 computed value is consistent with direct measurements inferred from the Camisea area
250 (~17°C/km; Figure 1b; Espurt et al., 2011) and the Tintaya mine (~14°C/km; Henry &
251 Pollack, 1988). Moreover, this value overlaps with compiled geothermal gradient values for
252 the Eastern Cordillera (Bolivia; 26±8°C/km; Barnes et al., 2008).

253 We thus convert cooling histories derived from QTQt expected models into
254 exhumation rates, using an assumed constant and spatially-uniform geothermal gradient of
255 18±4°C/km. Magmatic arc activity of the Abancay Deflection and its potential thermal
256 perturbation ceased after ~30 Ma (Mamani et al., 2010) and there is no evidence for posterior
257 reheating. For the surface, we implemented a lapse rate (temperature loss with altitude
258 increasing) of ~6°C/km according to Gonfiantini et al. (2001) for the eastern flank of the
259 inter-tropical Andes. Parameters used for QTQt data inversion are displayed in the Table S1.
260

261 **3.4 Thermo-kinematic modeling (Pecube)**

262 **3.4.1 Pecube**

263 Pecube is the only option, and presents the considerable advantage to simultaneously
264 test numerous tectonic or incision scenarios in 3D, computing thermal histories and to
265 confront numerical predictions to observed thermochronological data along altitudinal
266 profiles or for local data. Pecube computes thermal histories for rock particles at depth in
267 exhumation or burial contexts, taking into account landscape evolution (topography, relief),
268 the thermal regime of the crust, the tectonic settings (faults, uplift or subsidence) and isostasy
269 (Braun, 2003; Braun et al., 2012). Solving the 3D heat transfer equation in the crust, the
270 thermo-kinematic program Pecube v4.2 (Braun, 2003; Braun et al., 2012) predicts the spatial
271 distribution of thermochronological ages for specific samples considering exhumation
272 through lateral and vertical rock kinetics and relief evolution. We used Pecube in inverse
273 mode (Neighborhood Algorithm - NA; Sambridge, 1999a;b) to determine optimal value
274 ranges for tested parameters by minimizing the misfit function between predictions and
275 observations (Text S2).
276
277 **3.4.2 Input data and fixed parameters**
278 We processed thermochronological data including AFT and AHe thermochronometric
279 systems. We used 33 AHe ages (AHe mean grain ages, 28 new data and 5 from Gérard et al.,
280 submitted) and 42 AFT ages (AFT central ages, 32 new data, 2 from Kennan (2008) and 8
281 from Ruiz et al. (2009)). We implemented into Pecube present-day topography extracted
282 from the global elevation database GTOPO30 (Figure 5). He diffusion coefficient and AFT
283 annealing model from Farley (2000) and Ketcham et al. (1999) respectively have been
284 implemented into Pecube. For AHe data, we chose the Farley (2000) model for He diffusion
285 as it presents mean values for the diffusion coefficient for low-damaged apatites. In our case,
286 as exhumation histories are simple without identified reheating, damage influence plays a
287 minor role in the diffusion process. This model is identical to the Gautheron et al. (2009)

288 diffusion model in such a case. It is not possible with Pecube to reproduce the AHe age
289 dispersion between crystals due to damage impact on He diffusion (Gautheron et al., 2009;
290 Shuster et al., 2006). So, we here decided to implement the average ages and standard
291 deviation errors (Table S2). Regarding the AFT data, we also implemented track-length
292 measurements when available. Finally, Pecube model outcomes were also directly compared
293 to T-t paths derived from QTQt modeling.

294 In order to optimize computation time, we divided the Abancay Deflection into two
295 crustal blocks (Altiplano vs. Eastern Cordillera; Figure 2) that we modeled independently,
296 except for the exploration of the model thermal diffusivity vs. the basal temperature where
297 the Altiplano and the Eastern Cordillera were investigated together. Each of these crustal
298 blocks represents the natural tectono-morphic boundary of the Abancay Deflection. The
299 timespan explored starts at 50 Ma for all the simulations to eliminate any potential temporal
300 bias. We subsequently divided the explored timespan into six time slices: 50, 25, 15, 10, 5
301 and 0 Ma. For each time boundary, we fit the modeled mean paleo-elevation according to
302 Sundell et al. (2019). We do not have, however, any information regarding the relief
303 evolution of the Abancay Deflection that sits in a remote location never sampled before nor
304 any proxy for incision (Text S4). Finally, for exhumation rate quantification from
305 thermochronological data, we fixed the crustal thermal and rheological parameters in space
306 and time (Figure 5; Table S3). For these parameters, we finally explored the basal
307 temperature of the crustal block and the thermal diffusivity to test our chosen geothermal
308 gradient (Table S4).

309

310 **3.4.3 Neighborhood Algorithm inversions and explored parameters**

311 We used Pecube in inverse mode to quantitatively constrain parameter values
312 (tectono-morphic scenarios) that best reproduce the input thermochronological data. We

313 extracted the best-fitting parameter values for each inversion computing probability density
314 functions (Sambridge, 1999a;b). When the inversion clearly converges toward a unique
315 parameter solution (one peak for the probability density function), we extracted the parameter
316 value applying the 2σ standard deviation. We consequently used forward Pecube modeling to
317 present the best-fitting scenarios and data reproducibility using inversion-derived parameters
318 as input data (Supporting Information).

319 We first broadly explored the basal temperature and the thermal diffusivity to test our
320 geothermal gradient calculation (Table S4). Here, we investigated together the Altiplano and
321 the Eastern Cordillera crustal blocks. Because of computing time issues with the global
322 model, and as the Altiplano and the Eastern Cordillera present opposite morphologies (flat vs.
323 deeply incised; Gérard et al., submitted), and different exhumation trends according to local
324 studies (slow and continuous (Ruiz et al., 2009) vs. recent acceleration (Kennan, 2008;
325 Gérard et al. submitted), we explored these areas separately with the ultimate goal to unravel
326 the exhumation pattern. For the Altiplano model, we explored the basal crustal temperature
327 (proxy for the geothermal gradient; Figure 5), the exhumation history for the entire crustal
328 block (Figure 5), and landscape evolution through time (Topography offset and relief
329 amplification factor; Figure S38). For the Eastern Cordillera model, we explored the
330 exhumation history for the entire crustal block (Figure 5), relief and topographic evolution
331 (Figure S38), and the kinematics of the Apurimac fault system (fault dip, timing of initiation
332 and fault velocity; Figure 5). The detailed list of the explored Pecube parameters is available
333 in Table S4.

334 **Table 1**. Sample locations and bedrock lithologies

Sample number	Latitude (°S)	Longitude (°W)	Elevation (m)	Lithology	Geologic unit	Pluton age
Ocobamba profile*						
AB-17-05	13.091198	72.26337	3903	Granite	Mesapelada pluton	Permian
AB-17-06	13.07867	72.27952	3696	Granite	Mesapelada pluton	Permian
AB-17-07	13.07128	72.2803	3447	Granite	Mesapelada pluton	Permian
AB-17-08	13.05875	72.28962	3190	Granite	Mesapelada pluton	Permian
AB-17-11	13.00978	72.3299	2450	Monzonite	Mesapelada pluton	Permian
Individual data						
AB-17-13	12.83221	72.14085	1638	Granite	Colca pluton	Permian
AB-17-15	12.9652	72.07252	2475	Granite	Colca pluton	Permian
AB-17-18	12.64752	72.55498	912	Granite	Quellotuno pluton	Triassic
AB-17-19	12.89585	72.74471	1362	Granite	Kiteni pluton	Triassic
Lucma profile*						
AB-17-21	13.04408	72.88454	2235	Granite	Kiteni pluton	Triassic
AB-17-22	13.04171	72.93961	3020	Granite	Kiteni pluton	Triassic

Sample number	Latitude (°S)	Longitude (°W)	Elevation (m)	Lithology	Geologic unit	Pluton age
AB-17-23	13.02889	72.9593	3678	Granite	Kiteni pluton	Triassic
AB-17-25	13.00124	72.9468	4050	Granite	Kiteni pluton	Triassic
AB-17-26	13.03244	72.9577	3589	Granite	Kiteni pluton	Triassic
AB-17-28	13.05984	72.9371	2609	Granite	Kiteni pluton	Triassic
Limatambo profile*						
AB-17-29	13.5299	72.43471	4056	Diorite	Cotabamba pluton	Paleogene
AB-17-30	13.53367	72.45849	3795	Diorite	Cotabamba pluton	Paleogene
AB-17-31	13.5419	72.4688	3581	Diorite	Cotabamba pluton	Paleogene
AB-17-32	13.52771	72.4671	3322	Diorite	Cotabamba pluton	Paleogene
AB-17-33	13.51888	72.47569	2966	Diorite	Cotabamba pluton	Paleogene
AB-17-34	13.50543	72.4702	2740	Diorite	Cotabamba pluton	Paleogene
AB-17-35	13.50373	72.47325	2586	Diorite	Cotabamba pluton	Paleogene
AB-17-36	13.49839	72.48075	2435	Diorite	Cotabamba pluton	Paleogene
Abancay profile*						
AB-17-37	13.67147	72.89801	2800	Monzonite	Abancay orthogneiss	Triassic

Sample number	Latitude (°S)	Longitude (°W)	Elevation (m)	Lithology	Geologic unit	Pluton age
AB-17-38	13.67129	72.90512	2573	Diorite	Abancay orthogneiss	Triassic
AB-17-39	13.6721	72.90939	2280	Gabbro	Abancay orthogneiss	Triassic
AB-17-40	13.68018	72.91482	1916	Granite	Abancay orthogneiss	Triassic
AB-17-41	13.68651	72.84196	4136	Granite	Abancay orthogneiss	Triassic
AB-17-42	13.67414	72.85007	3753	Granite	Abancay orthogneiss	Triassic
AB-17-43	13.66636	72.86651	3459	Granitic arena	Abancay orthogneiss	Triassic
AB-17-44	13.6792	72.88035	3209	Granitic arena	Abancay orthogneiss	Triassic
Incahuasi profile*						
AB-17-51	13.2918	73.15121	3434	Granite	Chucuito pluton	Devonian
AB-17-55	13.30613	73.21085	2455	Granite	Chucuito pluton	Devonian

Note: The Geologic unit and pluton age columns refer to the studies of Egeler & De Booy (1961), Lancelot et al. (1978), Mišković et al. (2009), Perello et al. (2003), Reitsma (2012) and the INGEMMET geological database.

* Profile names were given considering the main cities nearby the investigated area.

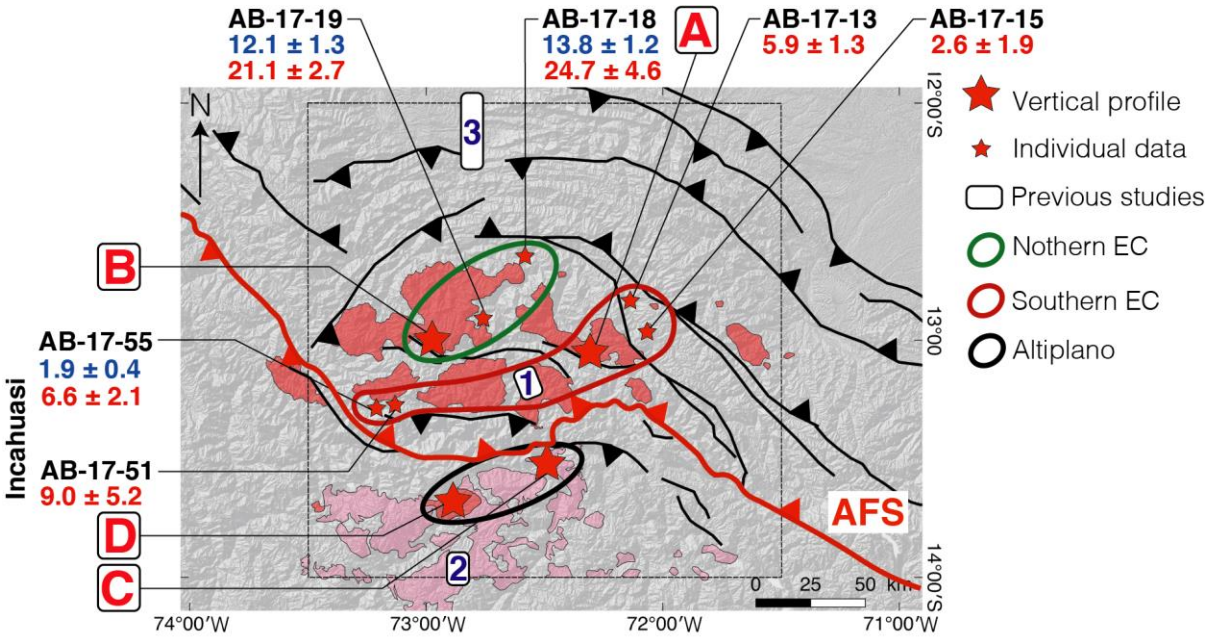

Figure 4. Sample locations of the new thermochronological ages within the Abancay Deflection. Red and pink polygons are respectively Permo-Triassic and Eocene plutons. Previous studies are: 1: Gérard et al. (submitted) and Kennan (2008); 2: Ruiz et al. (2009); 3: Espurt et al. (2011) and Gautheron et al. (2013). Blue and red numbers below sample names refer to AHe mean ages and AFT central ages for individual samples and the two-sampled-point Incahuasi vertical profile. Red capital letters refer to the other sampled vertical profiles (A: Ocobamba profile; B: Lucma profile; C: Limatambo profile & D: Abancay profile). Profiles results are displayed in Figure 6. Green, red and black contours mark the latitudinal segmentation of the Abancay Deflection defining three areas according to thermal histories modeled with QTQt (*i.e.* Northern EC, Southern EC and Altiplano respectively). The black dashed square frames the Abancay Deflection. AFT: Apurimac fault system; EC: Eastern Cordillera.

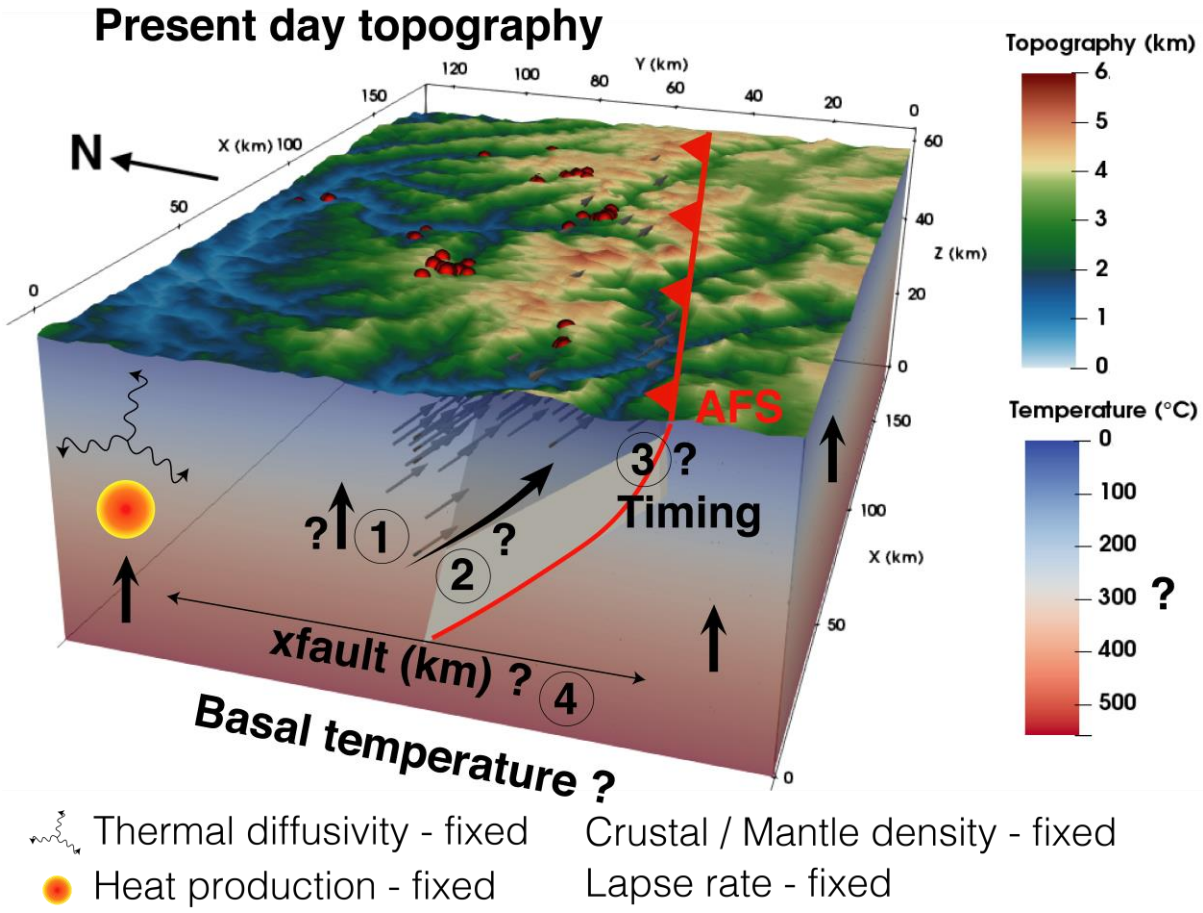

Figure 5. Parameters implemented and/or explored in Pecube through time. Example for the Eastern Cordillera crustal block (see Figure 2 for location). For the Altiplano block we only explored the crustal block exhumation (1). Red dots mark the location of the thermochronological data. Numbers and question marks refer to explored parameters. 1: Crustal block exhumation (km/Ma); 2: Fault velocity (km/Ma); 3: Timing of fault activation (Ma); 4: x fault (km), proxy for the fault geometry (fault dip). AFS: Apurimac fault system. Additional details are given in Table S4 & Figure S38.

4 Results

4.1 New thermochronological ages and AERs

For the entire Abancay Deflection area, the new 108 single-crystal AHe ages (from 28 samples) and the 27 AFT central ages range from 0.7±0.1 to 35.8±2.9 Ma and 2.6±1.9 to 38.2±4.4 Ma respectively, covering a temporal range from the late Eocene to the late Pleistocene (Figure 4 & 6; Tables 2 and 3). Reproducibility of single-crystal AHe ages is satisfactory with averaged dispersion < 10% for the whole dataset. For AFT central ages, all samples passed the χ^2 test (> 5%; Table 3; Figures S1 to S27), meaning that we can consider single-age populations for each sample (Green, 1981). Thermochronological ages ranging up to ~40 Ma are characteristic of the northern Eastern Cordillera and the Altiplano, as shown for the Lucma, Abancay and Limatambo altitudinal profiles and individual data (AB-17-19 and AB-17-18; Figure 4 & 6). The southern Eastern Cordillera presents much younger thermochronological ages, all <10 Ma (Ocobamba and Incahuasi profiles, AB-17-13 and AB-17-15; Figure 4 & 6).

For all altitudinal profiles, both AHe and AFT ages best fit a single AER, but they reveal different rates and timing of exhumation (Figure 6). The Lucma profile presents an apparent exhumation rate of ~0.1 km/m.y. between 40 to 0 Ma, while the Abancay and Limatambo profiles give apparent exhumation rates between 0.1 to 0.2 km/m.y. with a possible increase in exhumation since 10-15 Ma. The Ocobamba profile presents much higher apparent exhumation rates for the last 6 Ma, with $0.5^{+0.2}_{-0.1}$ km/m.y for AHe and $0.9^{+3.7}_{-0.4}$ km/m.y. for AFT. These exhumation rates values correspond to the lowest computed BIC and consequently the best-fitting solutions according to the Bayesian approach (Glotzbach et al., 2011).

4.2 Numerical thermo(-kinematic) modeling

Modeled Time-temperature paths with QTQt show for the entire study area a moderate and continuous cooling history with a cooling rate of ~2.5°C/m.y. between 40 and ~5 Ma (Figure 7). Even if cooling trends are relatively similar for the northern Eastern Cordillera and the Altiplano (Figures 7a and 7c; Figures S31 to S35), T-t paths for the southern Eastern Cordillera (Ocobamba profile and individual data) suggest an increase in cooling rate with values of ~17°C/m.y. between 7 and 3 Ma (Figure 7b; Figures S28 to S30 & S36), in agreement with AERs (Figure 6).

For Pecube modeling, we display results from our thermo-kinematic inversions in 2D graphics, where the explored parameter space is illustrated and each forward model is colored by its respective misfit value (Figures 8, 9 and 10). For the entire Abancay Deflection model, the basal temperature converges for values of 200°C to 700°C meaning geothermal gradient of 6°C/km to 23°C/km (Text S1). The thermal diffusivity however, does not converge (Figure 8). We present thereafter the best-fitting value for explored parameters within each modeled crustal block. For the Altiplano model, parameter exploration through data inversion reveals a clear inversion convergence for the output crustal-block exhumation rate at 0.2±0.1 km/m.y (Figure 9a) with high reproducibility for thermochronological ages and time-temperature paths (Figure 9b; Figure S41). The basal temperature does not converge but presents four peaks at 420±15°C, 480±20°C, 525±10°C and 675±30°C (Figure 9a) corresponding respectively to geothermal gradients of 14±1, 16±1, 17±1 and 22±1°C/km (Text S1). Relief amplification factors do not converge neither and are non-determinative or not discriminating (Figure S39). For the Eastern Cordillera model, the well-constrained value for crustal-block exhumation is converging to 0.2±0.1 km/m.y (Figure 10a), similarly to the Altiplano's results. The lateral (north-south) position of the Apurimac fault system at 25 km depth (x fault parameter) is constrained for an ideal value of -34±5 km (the negative sign corresponds to the northward exploration of this parameter). According to the approximate

surface trace of the Apurimac fault system and to the output of the x fault value, we estimated a fault dip ranging between 28° to 47° toward the north (Figures 10a and 10d). Regarding the fault kinetics, Pecube models favor fault activation at 5.3±1.5 Ma with an associated fault velocity of 2.9±0.6 km/m.y. (Figure 10b). According to our estimate on fault dip and velocity predictions, output exhumation rates of 1.2±0.4 km/m.y. are predicted for the southern Eastern Cordillera since ~5 Ma (Figure 10e). For the same time period, the northern Eastern Cordillera and the Altiplano underwent steady exhumation rates (Figure 11). Finally, and similarly to the Altiplano crustal-block model, relief amplification factor through time does not converge for the Eastern Cordillera model (Figure S40). The thermochronological data reproducibility is, however, excellent (Figure S42).

421

Table 2. Apatite (U-Th-Sm)/He data

Sample number	Morphology	Length (μm)	Width (μm)	Thickness (μm)	R_s (μm)	Weight (μg)	F_T	^{4}He (nccSTP/g)	^{238}U (ppm)	^{232}Th (ppm)	^{147}Sm (ppm)	Th/U	eU (ppm)	Age (Ma)	Corrected Age (Ma)	± 1 σ
Ocobamba profile																
AB-17-05A	2b	144	92	99	63	2.9	0.78	16932	29.3	21.5	80.5	0.7	35	4.1	5.2	0.4
AB-17-05B	2py	201	128	115	61	4.1	0.77	14156	40.5	25.2	84.6	0.6	47	2.5	3.3	0.3
AB-17-07A	1b + 1py	180	139	122	73	5.1	0.81	23568	65.6	41.9	98.1	0.6	76	2.6	3.2	0.3
AB-17-07B	2b	118	125	79	54	2.1	0.74	22253	45.1	26.1	93.4	0.6	52	3.6	4.9	0.4
AB-17-07C	2b	109	108	92	64	2.3	0.78	19309	58.3	35.4	107.4	0.6	67	2.4	3.1	0.2
AB-17-07D	2b	194	128	115	79	6.2	0.82	7087	36.2	26.3	92.8	0.7	43	1.4	1.7	0.1
AB-17-07E	1b + 1py	146	123	118	68	3.6	0.79	6820	32.2	20.5	82.4	0.6	38	1.5	1.9	0.2
AB-17-08A	2b	198	112	114	76	5.8	0.81	12131	63.8	29.1	88.9	0.5	71	1.4	1.7	0.1
AB-17-08B	1b + 1py	212	142	133	81	7.2	0.82	13951	70.6	18.7	89.3	0.3	76	1.5	1.9	0.1
AB-17-08C	1b + 1py	168	117	122	69	4.2	0.80	14539	56.3	27.4	85.2	0.5	63	1.9	2.4	0.2
AB-17-08D	1b + 1py	162	129	114	68	4.0	0.79	18175	59.2	19.0	81.6	0.3	64	2.4	3.0	0.2
AB-17-08E	1b + 1py	182	164	157	89	7.7	0.84	8668	47.2	17.1	72.9	0.4	52	1.4	1.7	0.1
AB-17-11A	1b + 1py	133	101	105	59	2.4	0.76	21106	111.0	213.5	89.7	1.9	163	1.1	1.4	0.1

Sample number	Morphology	Length (μm)	Width (μm)	Thickness (μm)	R_s (μm)	Weight (μg)	F_T	^{4}He (nccSTP/g)	^{238}U (ppm)	^{232}Th (ppm)	^{147}Sm (ppm)	Th/U	eU (ppm)	Age (Ma)	Corrected Age (Ma)	± 1 σ
AB-17-11B	2b	171	99	93	64	3.5	0.78	13654	65.5	157.8	72.5	2.4	104	1.1	1.4	0.1
AB-17-11C	1b + 1py	207	104	99	62	4.1	0.77	15283	107.9	190.1	76.6	1.8	154	0.8	1.1	0.1
AB-17-11E	2b	191	119	99	69	4.7	0.79	3626	29.4	55.0	27.3	1.9	43	0.7	0.9	0.1
Individual data																
AB-17-18A	2b	144	127	119	82	4.8	0.82	24984	10.8	39.4	40.9	3.6	21	10.2	12.4	1.0
AB-17-18B	2b	146	93	96	63	2.9	0.78	42585	19.6	68.4	52.4	3.5	36	9.8	12.7	1.0
AB-17-18C	2b	230	120	114	78	7.0	0.82	33557	12.0	41.1	37.7	3.4	22	12.8	15.6	1.3
AB-17-18E	2b	128	128	99	69	3.2	0.79	20493	8.3	27.5	35.9	3.3	15	11.4	14.4	1.2
AB-17-19A	2b	172	159	143	99	8.6	0.85	148729	122.7	5.9	55.9	0.1	124	9.9	11.6	0.9
AB-17-19B	2b	158	129	93	65	3.7	0.78	108144	103.9	11.9	48.2	0.1	107	8.4	10.7	0.9
AB-17-19I	2b	164	135	106	74	4.7	0.81	81674	58.3	4.8	32.2	0.1	60	11.3	14.0	0.8
Lucma profile																
AB-17-21A	1b + 1py	169	126	112	68	4.1	0.79	5878	50.8	144.1	61.4	2.8	86	0.6	0.7	0.1
AB-17-21C	2py	324	145	137	78	10.5	0.82	22398	55.6	290.9	91.1	5.2	126	1.5	1.8	0.1
AB-17-21D	2b	207	141	118	82	7.2	0.82	10613	35.4	102.9	40.6	2.9	60	1.5	1.8	0.1

Sample number	Morphology	Length (μm)	Width (μm)	Thickness (μm)	R_s (μm)	Weight (μg)	F_T	^{4}He (nccSTP/g)	^{238}U (ppm)	^{232}Th (ppm)	^{147}Sm (ppm)	Th/U	eU (ppm)	Age (Ma)	Corrected Age (Ma)	± 1 σ
AB-17-21E	1b + 1py	205	107	116	66	4.7	0.79	1580	4.7	15.7	5.3	3.3	9	1.6	2.0	0.2
AB-17-22B	1b + 1py	205	100	98	61	3.9	0.77	109443	72.5	16.5	83.3	0.2	77	11.8	15.4	1.2
AB-17-22C	2b	120	110	94	65	2.6	0.78	69585	47.1	87.0	103.1	1.8	68	8.5	10.9	0.9
AB-17-22D	2b	130	119	108	74	3.6	0.81	89394	60.5	14.5	71.9	0.2	64	11.5	14.3	1.1
AB-17-22E	1b + 1py	115	111	77	46	1.4	0.70	89806	71.4	14.5	56.4	0.2	75	9.9	14.2	1.1
AB-17-25A	2b	102	137	84	56	2.0	0.75	129728	39.0	3.5	80.0	0.1	40	26.9	35.8	2.9
AB-17-25C	2b	109	92	97	63	2.2	0.78	586257	183.9	18.4	104.7	0.1	189	25.7	33.2	2.7
AB-17-25D	2b	145	125	80	54	2.6	0.74	266746	82.9	19.7	93.8	0.2	88	25.2	34.0	2.7
AB-17-25E	1b + 1py	170	139	127	75	5.1	0.81	131857	47.2	7.5	43.2	0.2	49	22.2	27.4	2.2
AB-17-26A	2b	217	111	105	72	5.6	0.80	37130	17.4	5.0	67.6	0.3	19	16.4	20.5	1.6
AB-17-26C	2b	165	142	129	89	6.6	0.84	11233	9.0	3.3	42.7	0.4	10	9.5	11.3	0.9
AB-17-28A	2py	218	94	84	49	2.8	0.72	15300	40.8	142.5	69.7	3.5	75	1.7	2.4	0.2
AB-17-28B	2py	192	105	79	46	2.3	0.70	13444	23.5	90.8	55.5	3.9	46	2.5	3.5	0.3
AB-17-28C	1b + 1py	228	117	89	57	4.1	0.75	11401	34.8	125.5	57.5	3.6	65	1.5	1.9	0.2
AB-17-28D	2b	157	150	122	85	5.9	0.83	21690	93.9	77.5	56.6	0.8	113	1.6	1.9	0.2

Sample number	Morphology	Length (μm)	Width (μm)	Thickness (μm)	R_s (μm)	Weight (μg)	F_T	^{4}He (nccSTP/g)	^{238}U (ppm)	^{232}Th (ppm)	^{147}Sm (ppm)	Th/U	eU (ppm)	Age (Ma)	Corrected Age (Ma)	± 1 σ
AB-17-28E	1b + 1py	146	101	94	57	2.4	0.75	31059	31.3	121.4	59.5	3.9	61	4.3	5.7	0.5
Limatambo profile																
AB-17-29A	2b	173	109	100	69	4.1	0.79	46518	37.9	83.0	7.5	2.2	58	6.7	8.4	0.7
AB-17-29B	2b	151	132	114	79	4.8	0.82	44428	21.3	59.1	6.9	2.8	36	10.4	12.7	1.0
AB-17-29C	1b + 1py	165	92	89	54	2.5	0.74	37896	19.2	54.1	11.9	2.8	32	9.8	13.2	1.1
AB-17-29D	1b + 1py	140	116	103	61	2.8	0.77	42107	23.3	66.6	10.8	2.9	39	8.9	11.6	0.9
AB-17-29E	1b + 1py	149	110	112	64	3.2	0.78	19662	13.4	31.7	8.7	2.4	21	7.8	10.0	0.8
AB-17-30B	1b + 1py	148	92	84	52	2.1	0.73	31674	22.5	40.6	8.2	1.8	32	8.2	11.2	0.9
AB-17-30C	1b + 1py	170	133	104	64	3.8	0.78	29403	14.2	35.4	8.8	2.5	23	10.8	13.9	1.1
AB-17-31A	2b	189	104	114	72	4.9	0.80	12508	11.6	33.1	8.0	2.9	20	5.3	6.7	0.5
AB-17-31C	1b + 1py	153	112	99	60	2.9	0.77	10929	11.0	23.3	4.8	2.1	17	5.5	7.1	0.4
AB-17-31E	1b + 1py	185	103	100	61	3.6	0.77	14176	9.6	32.4	10.7	3.4	17	6.8	8.8	0.5
AB-17-32A	2b	140	114	103	71	3.6	0.80	12686	9.6	32.4	4.5	3.4	17	6.1	7.6	0.6
AB-17-32B	2b	140	111	106	73	3.7	0.80	17613	11.9	30.3	6.1	2.6	19	7.6	9.5	0.8
AB-17-33A	2py	155	109	100	50	2.2	0.72	8244	7.4	19.0	7.0	2.6	12	5.7	7.9	0.5

Sample number	Morphology	Length (μm)	Width (μm)	Thickness (μm)	R_s (μm)	Weight (μg)	F_T	^{4}He (nccSTP/g)	^{238}U (ppm)	^{232}Th (ppm)	^{147}Sm (ppm)	Th/U	eU (ppm)	Age (Ma)	Corrected Age (Ma)	± 1 σ
AB-17-33B	1b + 1py	161	152	175	85	6.4	0.83	13196	15.3	33.0	14.8	2.2	23	4.7	5.6	0.3
AB-17-33C	2b	175	115	102	71	4.5	0.80	19221	36.9	31.1	5.6	0.8	44	3.6	4.5	0.3
AB-17-33D	1b + 1py	234	118	103	66	5.2	0.78	25030	18.9	27.2	7.6	1.4	25	8.2	10.4	0.6
AB-17-33E	2b	133	119	104	72	3.5	0.80	13308	11.2	21.8	11.5	1.9	16	6.7	8.3	0.5
AB-17-34A	2b	154	118	113	77	4.6	0.81	12084	11.3	29.9	9.2	2.6	19	5.4	6.7	0.5
AB-17-34B	2b	155	152	126	87	6.2	0.84	7372	7.6	27.1	7.7	3.6	14	4.4	5.2	0.4
AB-17-34C	2b	179	127	134	87	6.7	0.83	7112	10.3	31.9	17.8	3.1	18	3.3	4.0	0.3
AB-17-34D	1b + 1py	139	93	95	55	2.2	0.75	5905	8.1	19.5	5.5	2.4	13	3.8	5.1	0.4
AB-17-34E	2b	180	104	97	67	4.0	0.79	5074	6.8	26.9	11.2	3.9	13	3.2	4.0	0.3
AB-17-35D	1b + 1py	203	122	97	62	4.1	0.77	5720	15.3	25.9	8.9	1.7	22	2.2	2.9	0.2
AB-17-35E	2b	142	104	96	66	3.1	0.78	12729	11.6	30.8	6.1	2.7	19	5.6	7.1	0.6
AB-17-36A	1b + 1py	142	103	105	60	2.7	0.77	9698	23.5	41.8	8.5	1.8	34	2.4	3.1	0.3
AB-17-36D	1b + 1py	160	108	100	60	3.0	0.77	5544	9.4	32.3	6.6	3.4	17	2.7	3.5	0.3
AB-17-36E	1b + 1py	186	128	123	74	5.2	0.81	3274	12.6	37.8	10.5	3.0	22	1.3	1.6	0.1

Abancay profile

Sample number	Morphology	Length (μm)	Width (μm)	Thickness (μm)	R_s (μm)	Weight (μg)	F_T	^{4}He (nccSTP/g)	^{238}U (ppm)	^{232}Th (ppm)	^{147}Sm (ppm)	Th/U	eU (ppm)	Age (Ma)	Corrected Age (Ma)	± 1 σ
AB-17-37A	2py	242	123	125	67	5.8	0.79	70766	88.7	113.0	23.4	1.3	116	5.1	6.4	0.5
AB-17-37B	2b	117	113	102	70	2.9	0.80	72471	82.8	104.3	22.2	1.3	108	5.6	7.0	0.6
AB-17-37C	1b + 1py	252	139	111	71	6.8	0.80	51165	63.5	75.0	12.2	1.2	82	5.2	6.5	0.5
AB-17-37D	1b + 1py	189	132	100	57	3.5	0.75	38099	44.3	45.9	18.3	1.0	56	5.7	7.6	0.6
AB-17-38A	1b + 1py	240	121	128	75	6.9	0.81	53821	50.9	59.8	15.8	1.2	65	6.8	8.5	0.7
AB-17-38B	1b + 1py	254	132	144	82	8.8	0.83	52415	52.3	56.4	16.8	1.1	66	6.6	8.0	0.6
AB-17-38C	2py	297	144	152	80	10.2	0.82	67076	70.5	75.4	18.4	1.1	89	6.3	7.6	0.6
AB-17-38D	1b + 1py	260	133	149	83	9.3	0.83	77615	74.9	87.9	19.9	1.2	96	6.7	8.1	0.6
AB-17-38E	1b + 1py	202	119	97	61	4.0	0.77	13309	21.2	40.3	13.1	1.9	31	3.6	4.6	0.4
AB-17-39C	1b + 1py	190	129	132	77	5.8	0.81	55767	61.8	41.0	27.6	0.7	72	6.4	7.9	0.6
AB-17-39D	2py	185	109	99	53	2.9	0.74	95376	116.8	113.2	19.5	1.0	144	5.5	7.4	0.6
AB-17-40A	1b + 1py	237	118	124	73	6.6	0.81	137948	171.0	73.7	33.9	0.4	189	6.1	7.5	0.6
AB-17-40B	2py	209	115	113	60	4.1	0.77	50558	68.0	69.9	28.2	1.0	85	4.9	6.5	0.5
AB-17-40C	1b + 1py	247	128	137	79	8.0	0.82	92739	112.4	67.5	28.2	0.6	129	6.0	7.3	0.6
AB-17-40D	2py	228	156	161	76	7.5	0.81	103926	113.9	73.5	28.6	0.6	132	6.5	8.1	0.6

Sample number	Morphology	Length (μm)	Width (μm)	Thickness (μm)	R_s (μm)	Weight (μg)	F_T	^{4}He (nccSTP/g)	^{238}U (ppm)	^{232}Th (ppm)	^{147}Sm (ppm)	Th/U	eU (ppm)	Age (Ma)	Corrected Age (Ma)	± 1 σ
AB-17-40E	1b + 1py	197	128	104	65	4.5	0.78	49030	70.7	42.0	14.7	0.6	81	5.0	6.4	0.5
AB-17-41A	1b + 1py	224	131	125	77	6.8	0.81	25929	13.0	21.9	17.4	1.7	18	11.8	14.5	1.2
AB-17-41B	1b + 1py	115	103	95	55	1.8	0.74	50384	18.0	17.6	10.3	1.0	22	18.8	25.3	2.0
AB-17-41C	2py	220	121	104	58	4.1	0.76	40105	19.7	21.8	16.2	1.1	25	13.3	17.6	1.4
AB-17-41D	2b	160	111	134	77	4.9	0.81	27300	10.1	26.9	17.6	2.7	17	13.7	16.8	1.3
AB-17-41E	1b + 1py	187	137	122	74	5.4	0.81	37150	23.1	9.4	5.2	0.4	25	12.1	15.0	1.2
AB-17-42A	2b	180	128	122	83	6.3	0.83	67778	44.1	34.7	13.7	0.8	52	10.7	12.9	1.0
AB-17-42B	2b	145	132	125	86	5.3	0.83	25104	18.5	20.0	22.4	1.1	23	8.9	10.7	0.9
AB-17-42C	2py	216	109	113	59	4.1	0.76	100130	68.3	52.9	14.8	0.8	81	10.2	13.4	1.1
AB-17-42D	1b + 1py	177	101	123	63	3.7	0.77	72476	48.0	28.3	11.8	0.6	55	10.9	14.1	1.1
AB-17-43A	1b + 1py	166	108	90	56	2.8	0.75	49427	40.8	7.3	12.7	0.2	43	9.6	12.8	1.0
AB-17-43C	2b	162	93	85	58	2.8	0.76	35909	33.7	5.4	19.1	0.2	35	8.5	11.2	0.9
AB-17-43D	2b	197	92	100	63	3.9	0.77	49624	45.3	25.0	20.1	0.6	52	8.0	10.3	0.8
AB-17-43E	2b	164	97	93	63	3.3	0.78	43734	52.5	20.7	10.1	0.4	58	6.3	8.1	0.6
AB-17-44A	1b + 1py	214	112	101	63	4.5	0.78	144444	129.5	14.1	13.7	0.1	133	9.0	11.6	0.9

Sample number	Morphology	Length (μm)	Width (μm)	Thickness (μm)	R_s (μm)	Weight (μg)	F_T	^{4}He (nccSTP/g)	^{238}U (ppm)	^{232}Th (ppm)	^{147}Sm (ppm)	Th/U	eU (ppm)	Age (Ma)	Corrected Age (Ma)	± 1 σ
AB-17-44B	1b + 1py	100	114	181	60	2.1	0.76	86599	83.7	19.7	7.7	0.2	88	8.1	10.6	0.8
AB-17-44C	2b	184	139	114	79	6.0	0.82	76257	76.9	12.9	9.1	0.2	80	7.9	9.6	0.8
AB-17-44D	1b + 1py	154	110	102	61	3.0	0.77	94100	95.5	39.5	18.5	0.4	105	7.4	9.6	0.8
AB-17-44E	2b	136	110	110	74	3.7	0.81	134264	88.5	52.8	17.6	0.6	101	11.0	13.6	1.1
Incahuasi profile																
AB-17-55A	1b + 1py	213	157	139	84	8.0	0.83	5526	21.0	37.7	40.6	1.8	30	1.5	1.8	0.1
AB-17-55B	1b + 1py	198	117	110	68	4.7	0.79	6030	28.8	47.5	47.3	1.6	40	1.2	1.6	0.1
AB-17-55C	2py	221	117	102	58	4.0	0.76	10533	32.4	50.0	51.4	1.5	45	2.0	2.6	0.2
AB-17-55D	2b	183	129	125	85	6.6	0.83	5988	21.5	36.6	52.4	1.7	31	1.6	2.0	0.2
AB-17-55E	1b + 1py	196	138	132	79	6.4	0.82	4848	27.3	41.8	43.6	1.5	38	1.1	1.3	0.1

Note: Morphology refers to the apatite geometry. 2py: 2 hexagonal pyramids; 2b: 2 broken faces; 1b + 1py: 1 broken face & 1 hexagonal pyramid (Brown et al., 2013). F_T is the alpha ejection correction factor and Rs is the sphere equivalent radius of hexagonal crystal (Gautheron et al., 2012; Ketcham et al., 2011).

425 **Table 3**. Apatite fission-track data

Sample number	n	ρ_s (10^5 cm^{-2})	N_s	ρ_i (10^5 cm^{-2})	N_i	ρ_d (10^5 cm^{-2})	$P(\chi^2)$	Dispersion (%)	Central age (Ma)	± 2 σ	U (ppm)	± 1 σ	n D_{par}	MDpar (μm)	n TL	MTL (μm)
Ocobamba profile																
AB-17-05	23	0.99	(140)	27.7	(3915)	12.0	100.0	0.0	5.9	1.1	35	2	88	1.09	6	11.43
AB-17-06	24	0.47	(69)	21.3	(3155)	12.0	99.3	0.1	3.6	0.9	27	1	82	1.12	3	12.34
AB-17-07	22	0.64	(90)	29.2	(4098)	12.0	84.6	0.4	3.6	0.8	36	1	68	1.27	5	10.92
AB-17-08	25	0.85	(136)	40.6	(6486)	12.0	93.6	0.2	3.5	0.7	51	2	106	1.16	12	11.48
AB-17-11	20	0.73	(79)	34.3	(3725)	12.1	99.7	0.1	3.5	0.8	43	2	96	1.30	1	9.8
Individual data																
AB-17-13	30	0.65	(106)	18.3	(3007)	12.1	100.0	0.0	5.9	1.3	23	1	66	1.24	5	10.76
AB-17-15	26	0.07	(9)	4.15	(568)	12.1	99.3	0.2	2.6	1.9	5	0	52	1.18	N.D.*	N.D.*
AB-17-18	25	1.01	(160)	6.82	(1081)	12.1	100.0	0.1	24.7	4.6	8	1	109	1.53	3	10.83
AB-17-19	25	4.32	(476)	34.2	(3762)	12.2	87.0	0.3	21.1	2.7	42	2	139	1.29	10	11.48
Lucma profile																
AB-17-22	22	3.98	(388)	33.7	(3285)	12.2	87.1	0.3	19.8	2.7	41	2	115	1.15	5	10.87
AB-17-23	18	6.79	(314)	46.4	(2090)	12.2	47.4	6.9	25.2	3.8	57	3	92	1.16	7	11.72

Sample number	n	ρ_s (10^5 cm^{-2})	N_s	ρ_i (10^5 cm^{-2})	N_i	ρ_d (10^5 cm^{-2})	$P(\chi^2)$	Dispersion (%)	Central age (Ma)	± 2 σ	U (ppm)	± 1 σ	n D_{par}	MDpar (μm)	n TL	MTL (μm)
AB-17-25	18	16.5	(901)	73.0	(3979)	12.3	51.7	4.0	38.2	4.4	89	3	121	1.80	7	13.59
AB-17-26	24	2.95	(286)	24.8	(2393)	12.3	99.9	0.1	20.2	3.0	30	1	117	1.21	7	11.64
Limatambo profile																
AB-17-29	19	4.97	(307)	24.8	(1532)	13.8	96.0	0.1	37.9	5.7	27	2	96	1.65	8	11.99
AB-17-31	20	1.52	(109)	10.6	(764)	13.8	94.6	0.3	27.1	5.9	12	1	116	1.32	3	12.15
AB-17-32	20	1.90	(133)	14.5	(1017)	13.9	98.5	0.1	24.9	5.0	16	1	151	1.42	2	11.69
AB-17-33	22	1.87	(159)	17.6	(1499)	13.9	93.1	0.2	20.2	3.8	19	1	117	1.19	3	12.46
AB-17-36	18	1.95	(120)	16.3	(1000)	14.0	66.4	0.6	23.0	4.8	17	1	70	1.30	3	10.68
Abancay profile																
AB-17-37	20	4.44	(244)	50.6	(2778)	14.0	100.0	0.1	16.9	2.6	54	2	103	1.24	3	12.10
AB-17-38	20	6.94	(647)	69.4	(6470)	14.0	100.0	0.0	19.3	2.3	74	2	113	2.15	18	12.43
AB-17-39	20	4.77	(506)	49.6	(5262)	14.1	99.9	0.1	18.6	2.4	53	2	102	1.57	5	11.38
AB-17-40	20	5.73	(532)	62.9	(5837)	14.1	92.2	0.1	17.6	2.2	67	2	80	1.47	7	10.94
AB-17-41	26	3.27	(544)	18.3	(3041)	14.1	99.9	0.1	34.6	4.3	19	1	118	1.42	N.D.*	N.D.*
AB-17-42	26	5.48	(764)	34.1	(4761)	14.1	87.2	0.6	31.1	3.6	36	1	137	1.46	7	11.72

Sample number	n	ρ_s (10^5 cm^{-2})	N_s	ρ_i (10^5 cm^{-2})	N_i	ρ_d (10^5 cm^{-2})	$P(\chi^2)$	Dispersion (%)	Central age (Ma)	± 2 σ	U (ppm)	± 1 σ	n D_{par}	MDpar (μm)	n TL	MTL (μm)
AB-17-44	25	5.15	(632)	44.6	(5477)	14.2	98.1	0.2	22.4	2.7	47	2	146	1.70	21	11.37
Incahuasi profile																
AB-17-51	14	0.45	(18)	9.66	(389)	14.2	12.7	44.0	9.0	5.2	10	1	32	1.41	N.D.*	N.D.*
AB-17-55	27	0.88	(64)	25.1	(1833)	14.2	9.0	39.1	6.6	2.1	26	1	108	0.98	6	10.71
Previous studies																
LK95/200[†]	30	N.R.[§]	N.R.[§]	N.R.[§]	N.R.[§]	N.R.[§]	46.5	N.R.[§]	2.2	0.5	N.R.[§]	N.R.[§]	N.R.[§]	N.R.[§]	N.R.[§]	N.R.[§]
LK95/202[†]	30	N.R.[§]	N.R.[§]	N.R.[§]	N.R.[§]	N.R.[§]	97.0	N.R.[§]	2.4	0.5	N.R.[§]	N.R.[§]	N.R.[§]	N.R.[§]	N.R.[§]	N.R.[§]
Pi6.1[#]	23	2.27	(456)	20.7	(4159)	11.0	10.0	N.R.[§]	22.5	N.R.[§]	23	2	40	2.68	41	11.21
Pi6.2[#]	16	1.55	(168)	13.8	(1491)	10.9	100.0	N.R.[§]	22.0	N.R.[§]	17	2	20	2.78	31	13.40
Pi6.3[#]	20	1.74	(323)	16.2	(3005)	10.8	99.5	N.R.[§]	20.8	N.R.[§]	18	1	44	2.87	37	14.04
Pi6.4[#]	20	0.69	(137)	6.21	(1242)	10.7	98.0	N.R.[§]	21.1	N.R.[§]	7	2	28	2.37	46	12.76
Pi6.5[#]	19	0.79	(148)	9.05	(1701)	10.6	100.0	N.R.[§]	16.5	N.R.[§]	10	2	43	2.55	34	13.13
Pi6.6[#]	20	1.04	(203)	12.0	(2354)	10.5	87.0	N.R.[§]	16.2	N.R.[§]	14	1	31	2.61	21	13.36
Pi6.7[#]	20	1.09	(141)	12.7	(1637)	10.4	93.0	N.R.[§]	16.0	N.R.[§]	16	2	23	2.72	35	12.89
Pi6.8[#]	20	0.86	(140)	10.2	(1662)	10.3	93.0	N.R.[§]	15.5	N.R.[§]	12	2	17	2.98	30	12.45

Sample number	n	ρ_s (10^5 cm^{-2})	N_s	ρ_i (10^5 cm^{-2})	N_i	ρ_d (10^5 cm^{-2})	$P(\chi^2)$	Dispersion (%)	Central age (Ma)	± 2 σ	U (ppm)	± 1 σ	n D_{par}	MDpar (μm)	n TL	MTL (μm)

Note: Fission-track age is given as Central Age (Galbraith & Laslett, 1993). Samples were counted dry with a BX51 Olympus microscope at 1250x magnification. Ages were calculated with the BINOMFIT program (T. A. Ehlers et al., 2005), using a zeta value of 275.18 ± 11.53 and the IRMM 540 uranium glass standard (15 ppm U). MDpar = mean Dpar value, MTL = mean track lengths of horizontally confined tracks.

*N.D. = no data

†Previous data (Kennan, 2008). For samples LK95/200 and LK95/202, elevations are respectively 3.1 and 2.1 km.

§N.R. = not reported

Previous data from Ruiz et al. (2009) for samples Pi6.1 (3.87 km); Pi6.2 (3.80 km); Pi6.3 (3.65 km); Pi6.4 (3.45 km); Pi6.5 (3.25 km); Pi6.6 (3.10 km); Pi6.7 (3.00 km); and Pi6.8 (2.85 km).

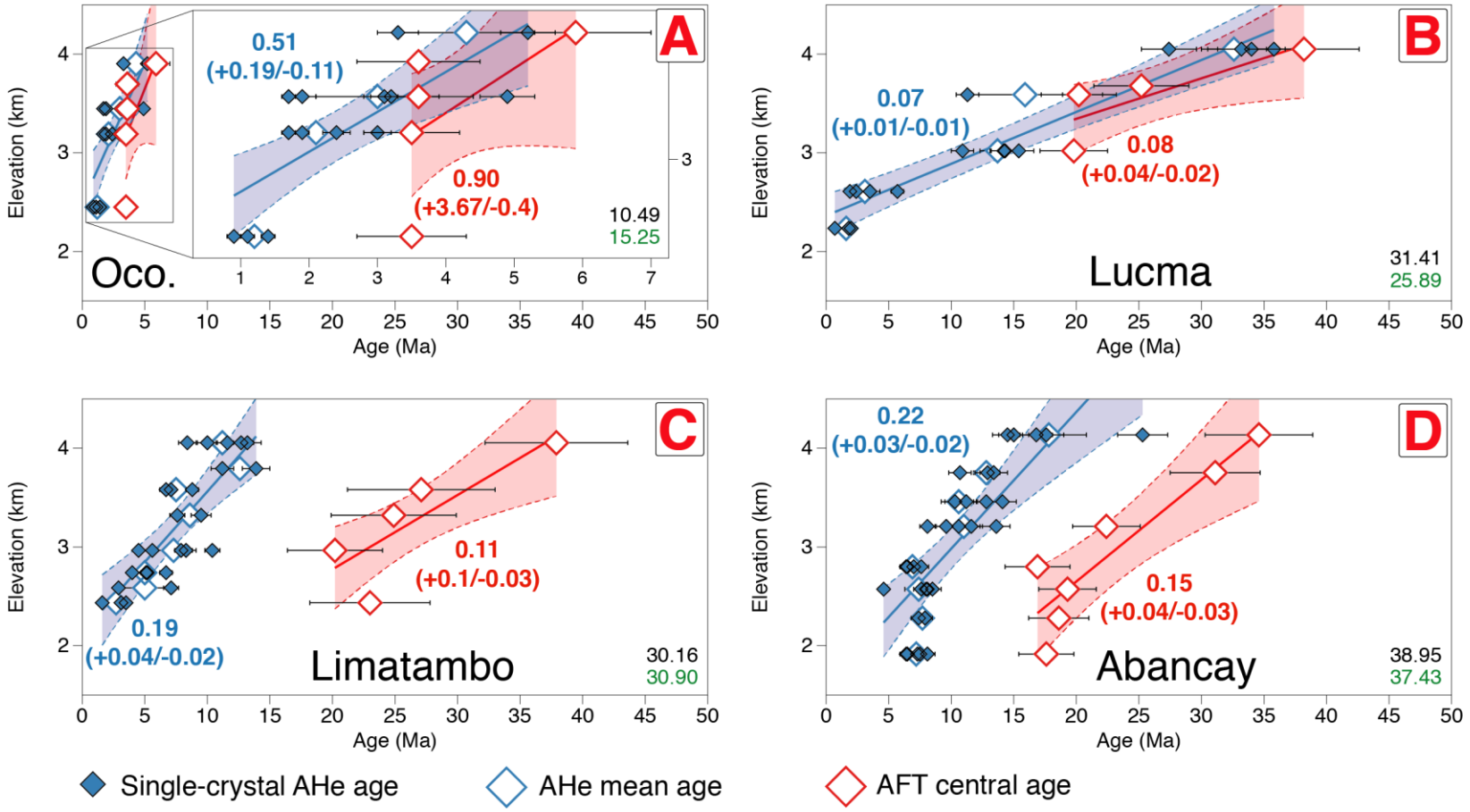

Figure 6. Age-Elevation plots (AHe & AFT ages) for the vertical profiles of Ocobamba (A; Oco.), Lucma (B), Limatambo (C) and Abancay (D) (see Figure 4 for profiles location). Blue diamonds are single-grain AHe ages, open diamonds are mean AHe (blue) and central AFT (red) ages. Blue and red numbers on the graphics refer to AER apparent exhumation rates (km/m.y.) respectively for AHe and AFT ages. Blue and red dashed lines correspond to minimum and maximum values for exhumation rates (AER; 95% confidence interval). BIC values for AHe and AFT data are respectively indicated in black and green on plots.

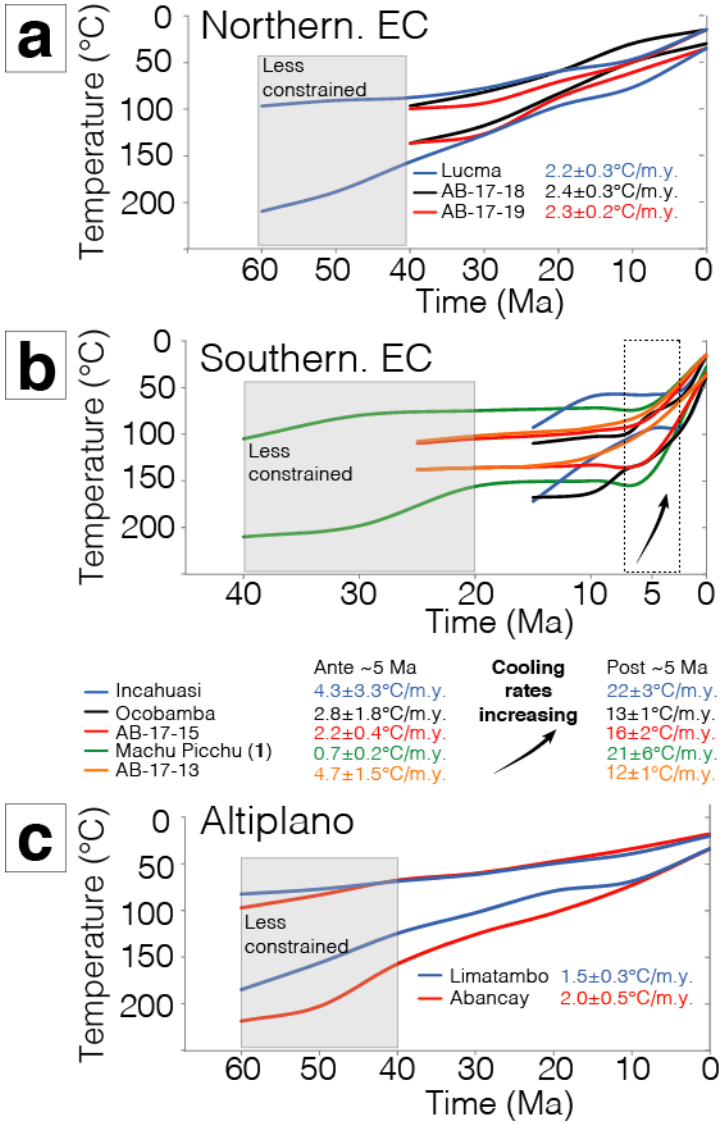

435

436 **Figure 7**. Time-temperature paths derived from QTQt inverse modeling of
437 thermochronological data (Gallagher, 2012). a, b and c: Synthesis of time-temperature paths
438 (colored lines) derived from QTQt (95 % reliability). Colored numbers in legend refer to the
439 output cooling rates. See the Supporting information for details regarding the data
440 reproducibility (observed vs. predicted data). a, b and c respectively correspond to samples in
441 the northern Eastern Cordillera (EC), the southern Eastern Cordillera and the Altiplano (see
442 Figure 4 for location). In b, number 1 (Machu Picchu profile) refers to Gérard et al.
443 submitted.

444

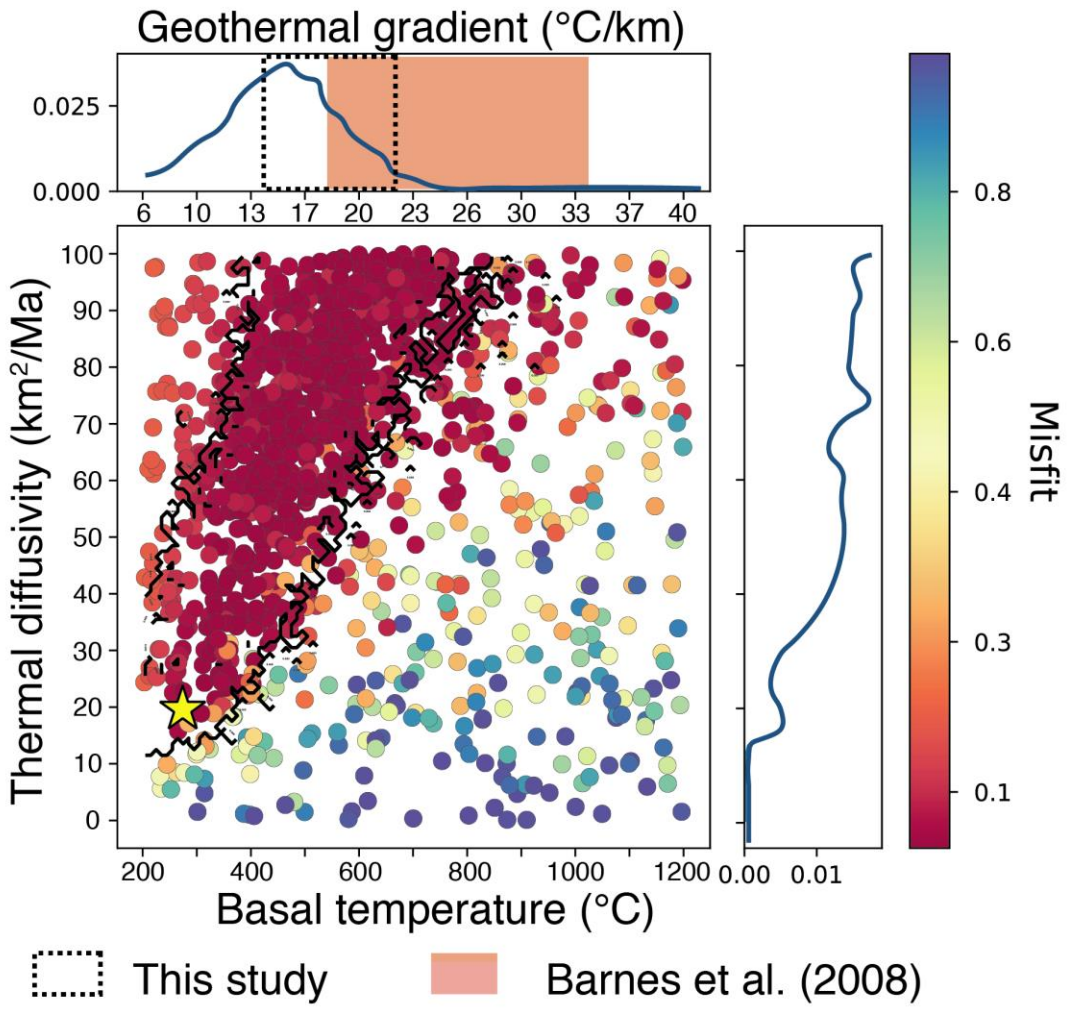

Figure 8. 3D Pecube inversion results regarding the thermal structure of the crust for the merged Altiplano and Eastern Cordillera crustal blocks. The graphic shows 2D parameter space and inversion results for thermal diffusivity vs. basal temperature. Each colored point corresponds to one forward model. The total sample size for inverse modeling is 1200. Blue curves (up and right subpanels) are the probability density for each parameter. The yellow star is the best-fitting model. The thermal diffusivity does not converge. We thus converted the basal temperature into geothermal gradients (Text S1) using a fixed thermal diffusivity of 40±11 km^2/Ma (compiled from Arndt et al., 1997 and Whittington et al., 2009). We compared these geotherms to our estimated range, and the one compiled by Barnes et al. (2008) (top panel).

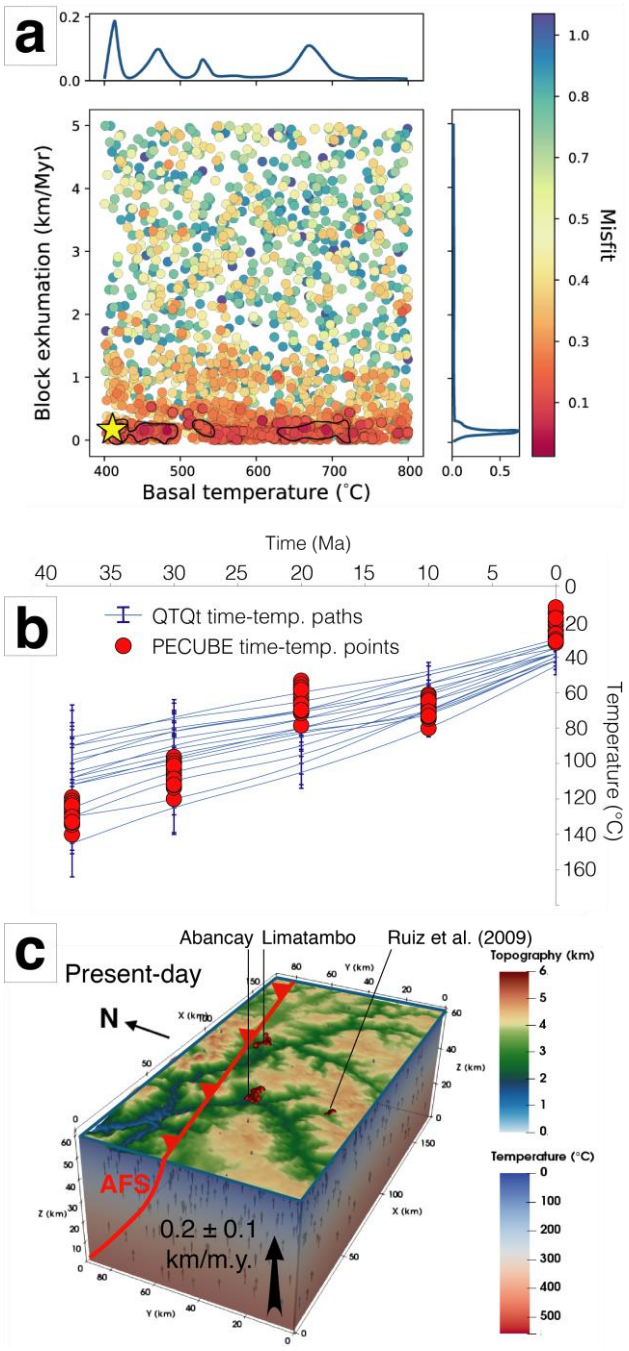

Figure 9. 3D Pecube inversion results for the Altiplano crustal block. a) 2D parameter space and inversion results for crustal-block exhumation vs. basal temperature. Each colored point corresponds to one forward model. Blue curves (up and right subpanels) are the probability density for each parameter. The yellow star is the best-fitting model. b) Direct comparison of time-temperature paths derived from QTQt and ones computed with Pecube best-fitting model. c) Crustal-block model for the Altiplano (see Figure 2 for location) with locations of thermochronological data.

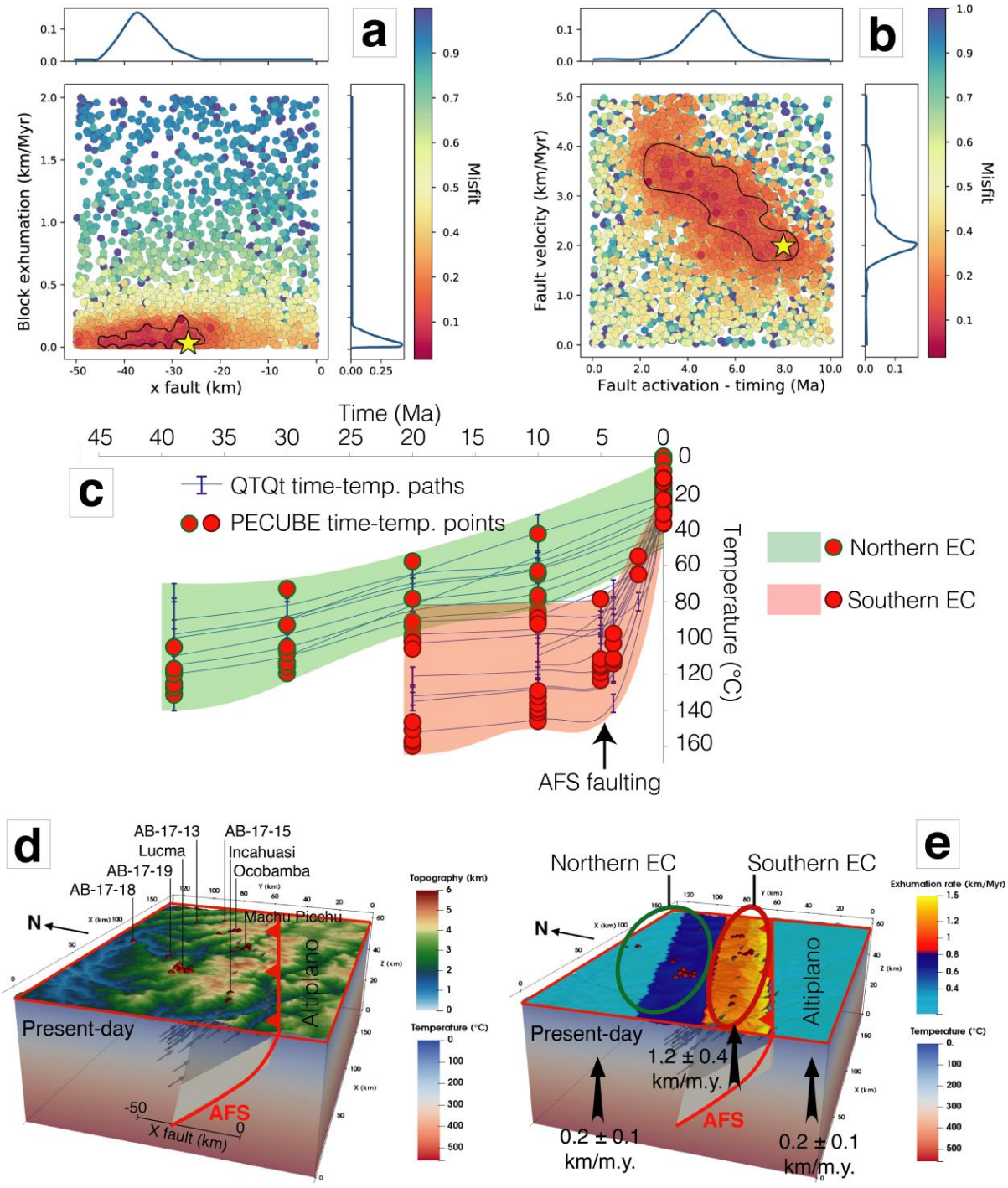

Figure 10. 3D Pecube inversion results for the Eastern Cordillera crustal block. a) 2D parameter space and inversion results for crustal-block exhumation vs. position of the fault at 25 km-depth (x fault parameter). b) 2D parameter space and inversion results for the fault velocity vs. activation timing of the Apurimac fault system. Each colored point corresponds to one forward model. Blue curves (up and right subpanels) are the probability density for

each parameter. The yellow stars in panels a and b are the best-fitting model. c) Direct comparison of time-temperature paths derived from QTQt and ones computed with Pecube best-fitting model. d) Crustal-block model for the Eastern Cordillera with locations of thermochronological data (see Figure 2 for location). e) Surface exhumation pattern for the Eastern Cordillera since ~5 Ma predicted from Pecube best-fitting model. AFS is the Apurimac fault system.

5 Discussion

5.1 From cooling rate to exhumation rate

Modeled thermal histories obtained from the Abancay Deflection area present only a monotonic cooling phase with variable cooling rates (Figure 7). Those thermal histories do not record any reheating event (Figure 7), which simplifies our modeling approach regarding the crustal thermal structure. This confirms that the thermal perturbation supposedly associated with the magmatic arc activity between 50 and 30 Ma (Mamani et al., 2010) is not registered in our local thermochronological record. This can be explained by three reasons: 1) present-day outcropping rocks were at that time still at depth and thus above the PRZ/PAZ, not impacted by this reheating event; 2) for the southern Eastern Cordillera, the high exhumation rates may have erased any older thermal signal; and 3) the thermal perturbation was potentially spatially and/or temporally localized and did not affect our sampled sites.

Because we did not detect any perturbation of thermal histories by reheating or potential isotherm relaxations (the sampled rocks were deep enough at that time), we convert the inferred cooling scenario into simple exhumation histories. Exhumation rates estimated using the obtained cooling rates derived from QTQt thermal modeling using a steady and spatially-uniform geothermal gradient (18±4°C/km), apparent exhumation rates from AERs (Glotzbach et al., 2011) and Pecube inversions results present consistent exhumation values

and high data reproducibility between three independent approaches (Figure S43). This confirms that the assumed geothermal gradients for QTQt and Pecube models are satisfactory, even if we cannot tightly constrain the basal crustal temperature from Pecube inversion (Figures 8 and 9a). This non-convergence issue is frequently encountered in this type of modeling (*e.g.* Robert et al., 2011; Valla et al., 2012) and can be bypassed only by imposing thermal parameter values that fit the regional geothermal gradient. In details, we notwithstanding identified four temperature peaks (probability density function for the Altiplano model; Figure 9a), corresponding to geothermal gradients spanning from 13°C/km to 23°C/km, compatible with the one we computed of 18±4°C/km, and the one obtained inverting thermal parameters for the entire Abancay Deflection (Figure 8). We furthermore performed inversion of given parameters for each crustal model (Altiplano and Eastern Cordillera blocks; Table S4; Text S5), imposing a "warmer" geothermal gradient (30°C/km; Text S5). It clearly appears that the ~20°C/km geothermal gradient seems to be the most likely option for the Abancay Deflection at the scale of our study with better thermochronological data reproducibility (Text S5; Figures S45 and S46).

We separated the study area in three zones derived from the exhumation rate output patterns (QTQt; Figure 4 and 7). Using results obtained from Pecube, the Altiplano and the northern Eastern Cordillera experienced similar exhumation histories since 40 Ma with exhumation rates of ~0.15±0.10 km/m.y. (Figure 11). The southern Eastern Cordillera experienced the same exhumation rate from ~20 to 5.3±1.5 Ma, followed by an acceleration of exhumation to 1.2±0.4 km/m.y. (Figure 11). Even though the thermochronological-data modeling and output time-temperature paths from QTQt are limited to the last 20 Ma for the southern Abancay Deflection (Figures 7b and 10c), we propose by temporal extrapolation that the southern Eastern Cordillera underwent similar exhumation rates as its neighboring areas (*i.e.* Altiplano and northern Eastern Cordillera) between 40 and 20 Ma. Over the last ~5

521 Ma, the exhumation acceleration is spatially framed southward by the Apurimac fault system,
522 pointing towards a differential exhumation pattern in the Abancay Deflection that we
523 attribute to tectonically driven surface uplift along the Apurimac fault system, and removal of
524 rocks by erosion.
525
526

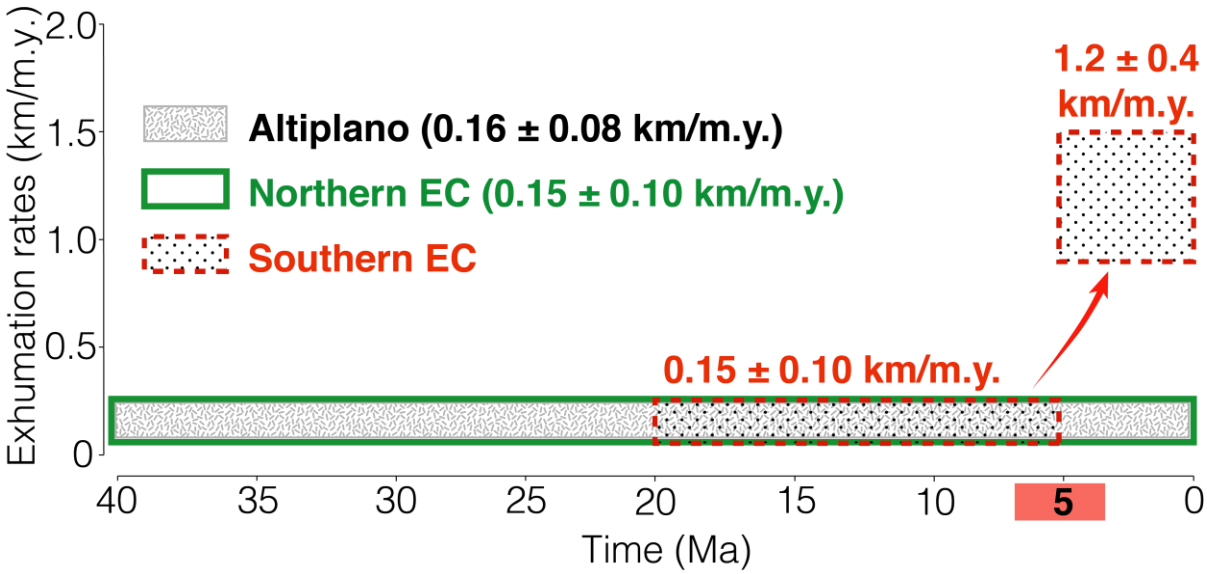

527
528 **Figure 11**. Exhumation rates derived from Pecube for the Abancay Deflection through time.
529 Each color corresponds to the three exhumation areas identified in this study. Details
530 regarding the computed values for exhumation rates according to AERs, QTQt and Pecube
531 are available in the Figure S43.
532
533 **5.2 Exhumation of the Abancay Deflection between 40 and 5 Ma**
534 The whole Abancay Deflection region experienced steady, moderate (0.2±0.1
535 km/m.y) and apparently spatially uniform exhumation between 40 and 5 Ma (Figures 11 and
536 12). This exhumation rate is highly consistent with those inferred between 40 and 15 Ma
537 from the only thermochronological data available in the area (0.17 km/m.y.; Ruiz et al.,
538 2009). Even if the Peruvian Altiplano experienced Miocene faulting delimitating intra-

539 mountainous basins (Tinajani, Punacancha, and Paruro basins; Carlotto, 2013; Horton et al.,
540 2014), there is no evidence for any acceleration of exhumation related to these crustal
541 processes. Surprisingly, although the Bolivian Eastern Cordillera registered peaks of
542 exhumation through tectonic and erosional processes between 50 and 15 Ma (Barnes et al.,
543 2012), our data and inverse models favor a large-scale uniform exhumation history during
544 that period.

545 Consequently, we interpret the steady and uniform exhumation rates as the record of
546 low-magnitude surface denudation affecting the Abancay Deflection in an internally-drained
547 environment (Figure 12). Furthermore, contemporaneously to the Bolivian Orocline bending
548 during Miocene (Roperch et al., 2006), the Abancay Deflection was built in a left-lateral
549 transpressional context (Dalmayrac et al., 1980) associated to lateral rock advection from the
550 south (Figure 12c and 12d). The crustal tectonic regime, dominated by horizontal motion,
551 cannot be registered by the thermochronological data, nor easily-modeled by balanced cross-
552 section that encompass only 2D processes (Gotberg et al., 2010). Moreover, our outcomes
553 pointing towards a low-magnitude exhumation rate of ~0.2 km/m.y. between 40 and 5 Ma are
554 comparable in term of magnitude with the large-scale and steady surface uplift (at ~0.1
555 km/m.y) of the Eastern Cordillera and the Altiplano modeled by Sundell et al. (2019). These
556 values are too close from each other to identify each component. We can, however, say that
557 the area did experience surface uplift (Sundell et al., 2019), meaning that erosion had been
558 less important than rock uplift. The exhumation rates we obtained are the part of rock uplift
559 accommodated by erosion, while the remaining part (unconstrained by our
560 thermochronological record) was the surface uplift.

561 These observations are compatible with large-scale tectonic shortening (Lamb, 2011;
562 Phillips et al., 2012) and/or lower crustal flow (Husson and Sempere, 2003; Tassara, 2005;
563 Ouimet and Cook, 2010). We cannot, however, exclude more rapid surface uplift of the

564 northern Altiplano between 10 and 5 Ma (0.4 km/m.y as suggested by Kar et al., 2016).
565 Indeed, in a potentially endorheic context (Gérard et al., submitted), sediment evacuation and
566 thus large-scale erosion rates are low. Consequently, the Altiplano may have risen rapidly
567 without prominent incision and thus recorded limited exhumation (*i.e.* steady low exhumation
568 rates despite rapid surface uplift, as already indicated by our limited exhumation rates).
569 Nevertheless, it has been also demonstrated from regional-climate numerical modeling that
570 such a surface-uplift acceleration can be an artifact driven by the climatic variability (Ehlers
571 & Poulsen, 2009). We thus favor the conservative hypothesis of a steady, slow and
572 continuous surface uplift and low associated exhumation rates between 40 and 5 Ma. As a
573 result, and based on our thermochronological data, we also discard the potential implication
574 of one or multiple lithospheric delamination event(s) implying pulses of rapid surface uplift
575 during the Miocene (Garzione et al., 2017).
576
577 **5.3 Southern Eastern Cordillera – 5 Ma exhumation rate increase**
578 The southern Eastern Cordillera framed southward by the Apurimac fault system
579 registered an order-of-magnitude acceleration of exhumation since ~5 Ma, driven by both
580 topographic incision and tectonic uplift (this study; Gérard et al., submitted). The local 5-Ma
581 exhumation event affecting the southern Eastern Cordillera (Figure 12e) cannot be explained
582 by large-scale phenomenon such as lithospheric delamination, neither in terms of spatial
583 extent nor timing (Garzione et al., 2006; Sobolev and Babeyko, 2005). Only tectonic uplift
584 along local structures associated with erosion could explain our observed pattern of
585 thermochronological ages and exhumation (Figure 4, 6 and 7). Pecube inverse outcomes
586 show that the inherited crustal-scale Apurimac fault system can reproduce the 3D
587 thermochronological-data pattern, with significant tilting of the southern Eastern Cordillera
588 (Figure 10). In such a deflected thrusting pattern, it is geometrically difficult to link the

589 southern Eastern Cordillera to a ramp located beneath and connected to the Subandean front.
590 Furthermore, the Subandean front has been active since 14 Ma (Espurt et al., 2011), which
591 clearly predates the 5-Ma exhumation signal we observed in the Eastern Cordillera. The
592 Apurimac fault system appears to be the most likely structure tilting the Eastern Cordillera
593 (Figure 10) associated to backthrusting activity with a relatively low north-dipping angle of
594 30-40° (Figure 10d).

595 Considering end-member values of best-fit Pecube parameters (*i.e.* fault dipping
596 angle, timing for fault activation and fault velocity), we estimated total horizontal crustal
597 shortening ranging between 6 and 21 km (mean shortening rate of 2.8±1.5 km/m.y.). The
598 total amount of vertical rock uplift ranges between 4 and 17 km (mean rock uplift rate of
599 2.2±1.3 km/m.y.) since 5 Ma. The parameter ranges derived from our approach do not allow
600 to constrain precisely the tectonic deformation (nor vertical or horizontal) rates and thus to
601 further discriminate the tectonic balance and the respective importance of different rock uplift
602 drivers for the southern Eastern Cordillera. On the other hand, vertical tectonic uplift rates
603 overlap exhumation rates over the last 5 Ma (2.2±1.3 km/m.y. vs. 1.2±0.4 km/m.y.
604 respectively; Figure 11), which highlights the consistency between 2D and 3D modeling
605 approaches. Furthermore, constrained 5-Ma horizontal shortening rates for the southern
606 Eastern Cordillera (2.8±1.5 km/m.y.) are also consistent with balanced cross-section
607 reconstructions and derived shortening rates in the Subandean area (~3.8 km/m.y.; Espurt et
608 al., 2011), directly located to the north of the Abancay Deflection (Figure 1).

609 Although thick-skinned backthrusts have been reported as active since the late-
610 Miocene to the north of the Abancay Deflection (Shira mountains; Gautheron et al., 2013;
611 Wimpenny et al., 2018; Huaytapallana fault, in the continuity of the Apurimac fault system;
612 Dorbath et al., 1990; Figure 3b), we document for the first time the recent tectonic activity
613 (*i.e.* <5 Ma) for the Abancay region itself, with significant but local exhumation through the

614 Apurimac fault system south-verging backthrusting. The low-magnitude earthquakes cluster
615 in this zone (Figure 3a) strongly corroborates our interpretation, also supporting the
616 hypothesis that such fault activity and observed exhumation pattern on million-year
617 timescales is still ongoing today.
618
619 **5.4 Potential drivers for the Apurimac fault system re-activation**
620 The Abancay Deflection is framed northward by the Subandean zone, which has been
621 tectonically active since ~14 Ma (Espurt et al., 2011). To the south, the Altiplano is
622 characterized by extensional faulting since the Quaternary (Sébrier et al., 1985; Wimpenny et
623 al., 2018). Our results show that the Eastern Cordillera was tilted through the south-verging
624 backthrust of the Apurimac fault system, which has been active since ~5 Ma (Figures 12e and
625 13). Considering the orogenic-prism balance theory (Whipple & Meade, 2004; Willett et al.,
626 1993), the tectonic-shortening transfer from the Altiplano to the Subandes (since ~15 Ma in
627 Bolivian Andes; Horton, 2005; Norton and Schlunegger, 2011; Anderson et al., 2018) was
628 triggered by sediment accumulation in the foreland basin (i.e. paleo-Subandean zone; Mosolf
629 et al., 2011) following the late-Miocene South-American monsoon intensification (Poulsen et
630 al., 2010). Thus, the question of the out-of-sequence Apurimac back thrust activity needs to
631 be addressed.
632 From a morphologic viewpoint, the peculiarity of the Abancay Deflection is that this
633 is the only region at the scale of the Altiplano where the hydrographic network is reaching
634 the core of the orogen after crossing the entire Eastern Cordillera (Apurimac and Urubamba
635 Rivers; Figures 1 and 12). The river capture, incision and subsequent increased denudation
636 was probably triggered and enhanced by wetter conditions during the late-Miocene (Poulsen
637 et al., 2010) and the Pliocene climate variability (Lease & Ehlers, 2013; Peizhen et al., 2001).
638 Given its reverse faulting timing initiation at ca. 5 Ma, the Apurimac fault system has played

as an out-of-sequence thrust. We thus conceptually interpret in the following the tectonic evolution of the Abancay Deflection (Figures 12 and 13), linking the climate evolution and the tectonic transfer regarding the orogenic prism rebalancing and geodynamic settings:

(1) Late-Miocene precipitation intensification (Poulsen et al., 2010) on the eastern flank of the Peruvian Andes favored the regressive erosion through the proto-Apurimac and -Urubamba Rivers. These paleo-drainage systems captured and incised the internally-drained paleo-Abancay Deflection (Figures 12d and 12e).

(2) Consequently, this drainage capture and river incision subsequently enhanced denudation processes over the large-scale Abancay Deflection. Rivers deeply carved the Eastern Cordillera, sediments were exported toward the foreland basin and trapped within it (paleo-Subandes).

(3) By orogenic prism rebalancing, the Subandean deformation propagated northward at ~5 Ma (Mosolf et al., 2011; Gautheron et al., 2013). In the core of the orogen, mass removal favored tectonically driven surface uplift of the eroding southern Eastern Cordillera through the Apurimac fault system (Figures 12e and 13).

(4) Focused deformation localized on the Apurimac fault system may be explained by its peculiar position at the northern edge of the Arequipa terrane (Figure 13; Loewy et al., 2004). The south-verging Apurimac fault system plays the role of a buttress on which the north-verging Subandean thrust ramp is rooted, forming a crustal-scale flower structure with the underplated Arequipa terrane southward and the Brazilian shield northward (Figure 13). The northward advance of the Arequipa terrane is still an ongoing process according to GPS measures that favor the current Bolivian Orocline bending (Allmendinger et al., 2005). Complementarily, the Apurimac fault system is a lithospheric-scale inherited structure (Carlier et al., 2005; Dalmayrac et al., 1980; Sempere et al., 2002) and constitutes a mechanical weak zone promoting the localization and accumulation of deformation.

Although the Andes present numerous deflected zones (*i.e.* Cajamarca, Huancabamba in Peru; Dalmayrac et al., 1980), the Abancay Deflection is exceptional with respect to its size, highly-rotated fault systems and its peculiar location at the northern tip of the Altiplano. It marks abruptly the along-strike segmentation of the Central Andes facing the Amazonian basin with E-W topographic high. Even if backthrusting activity through reactivated Cretaceous crustal normal fault tilting in the Eastern Cordillera is already documented in southern Peru (Perez et al., 2016), the Apurimac fault system backthrusting is abnormal and unique. To our knowledge, there is nowhere else in the Andes a crustal-scale and even a probable lithospheric-scale inherited structure (Carlier et al., 2005; Sempere et al., 2002) and suture between the eastern Altiplano and the Eastern Cordillera reactivated as a backthrust within the last 5 Ma providing stronger uplift in the Eastern Cordillera. The relative position of the Arequipa terrane (Figure 12) acting as a rigid indenter (Gérard et al. submitted) could explain the accumulation of horizontal and vertical deformation in such limited-extend area and the subsequent orthogonal direction of the topography in comparison to the main orogen elongation axis. This could furthermore explain this undocumented-before tectonic behavior and probable higher erosion rates with an E-W topography facing the Amazonian moisture flux enhancing orographic updraft.

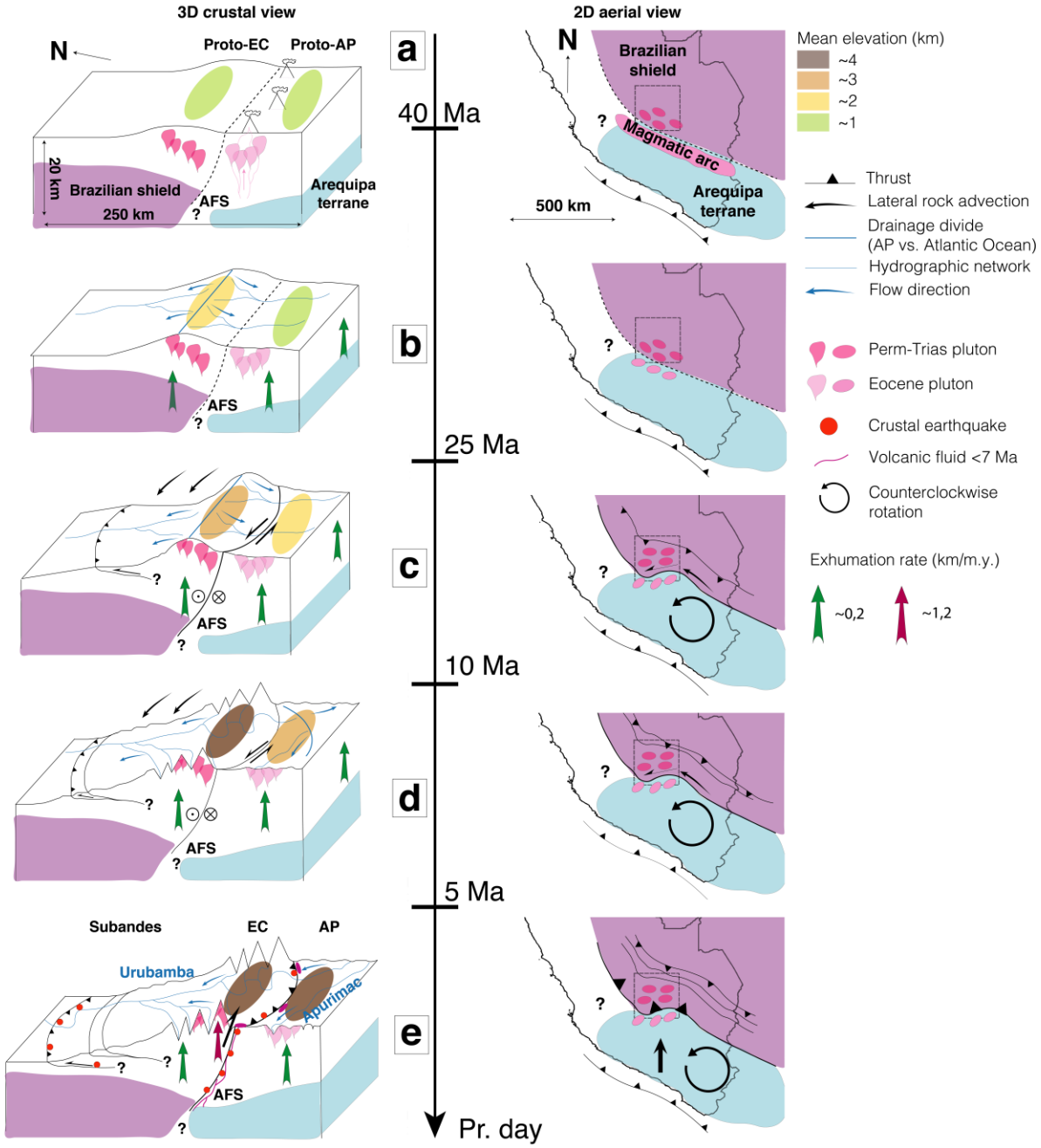

Figure 12. Tectonomorphic evolution of the Abancay Deflection since 40 Ma. Right panels represent the large-scale schematic aerial views of the study area (black dashed square). Left panels are 3D Abancay Deflection schematic crustal blocks corresponding to the surface to the square defined in the right panels. a, b, c, d and e refer respectively to the situation at 40 Ma, between 40 and 25 Ma, between 25 and 10 Ma, between 10 and 5 Ma and finally since 5 Ma to present day. AFS: Apurimac fault system; EC: Eastern Cordillera; AP: Altiplano.

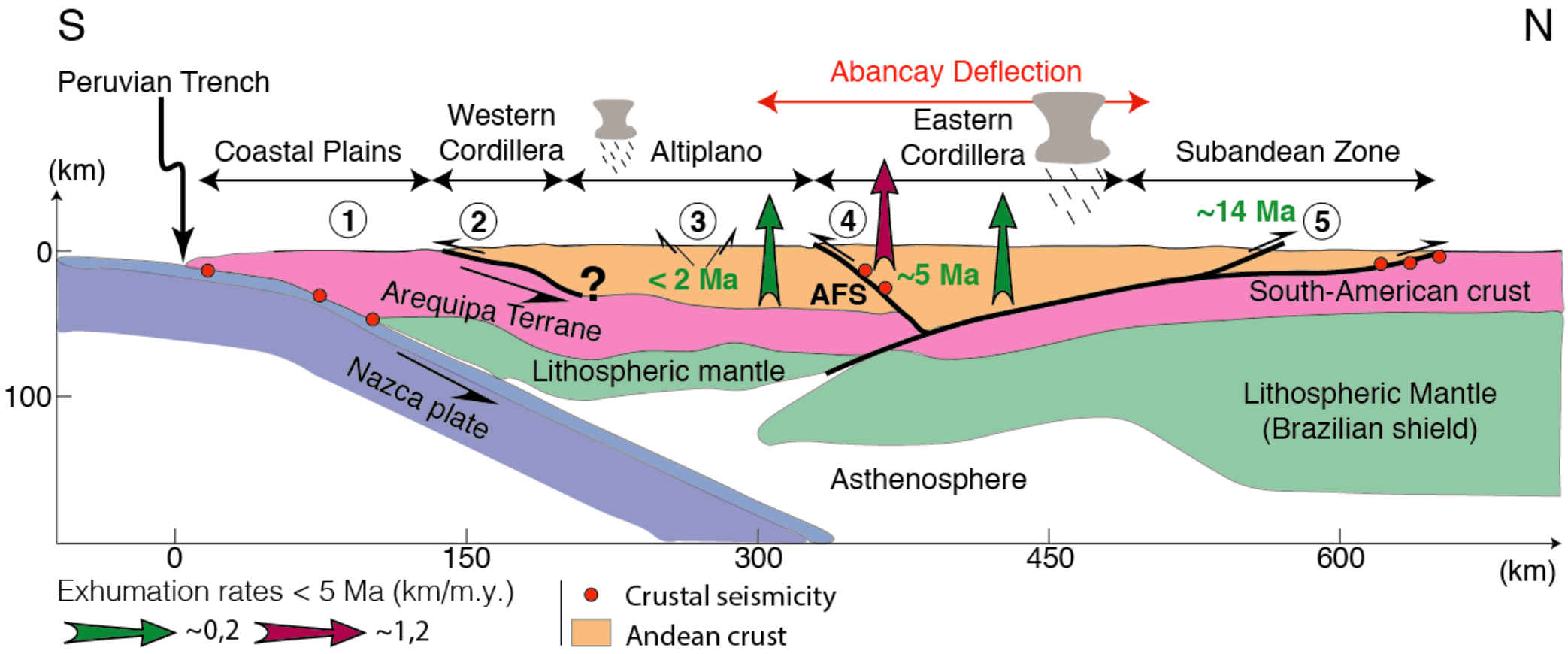

Figure 13. Andean orogenic model (South-North cross section) crossing through the Abancay Deflection since ca. 5 Ma. Modified after the double-verging prism orogenic model of Armijo et al. (2015). Green numbers refer to the initiation timing of the associated crustal deformation. Black circled numbers refer to the compiled previous and present studies: 1: Loewy et al. (2004); Ramos (2008, 2010); 2 : Armijo et al. (2015); 3: Sébrier et al. (1985); Mercier et al. (1992); Wimpenny et al. (2018); 4: This study; 5: Espurt et al. (2011); Gautheron et al. (2013). AFS refers to Apurimac Fault System.

694 **5.5 Is the Abancay Deflection a Tectonic syntaxis?**

695 The Abancay Deflection presents numerous geomorphic, tectonic and geodynamic
696 features behind the theory of the tectonic syntaxes (Table 4) already documented in the
697 Himalaya (Namche Barwa; Nanga Parbat; e.g. Zeitler et al., 2001) and Alaska (Saint Elias
698 mount; *e.g.* Enkelmann et al., 2017). Focusing on the Abancay Deflection, high exhumation
699 rates concentrated in the core of a distorted zone of limited-extend and framed by deflected
700 active faults, promote the classification of the Abancay Deflection as a tectonic syntaxis
701 (This study; Table 4). In this case, the Arequipa terrane could play the role of the indenter in
702 response to counterclockwise rotation (Roperch et al., 2006) of the northern limb of the
703 Bolivian Orocline since the Miocene (Allmendinger et al., 2005; Müller et al., 2002).

704 The Himalayan syntaxes are characterized by heat advection, subsequent upward
705 deflection of isotherms inducing a brittle-ductile rheological limit to the ascent (Koons et al.,
706 2013). These peculiar thermal and rheological parameters associated to high geothermal
707 gradients (~60°C/km; Craw et al., 1994) and shallow seismicity (~2-5 km depth; Meltzer et
708 al., 1998) are defining tectonic aneurisms (Koons et al., 2013). The Abancay Deflection,
709 however, seems to be relatively "cold" (~20°C/km; this study) and deeply brittle with poorly-
710 documented geothermal gradient measurements that rarely exceed 30°C/km (Eastern
711 Cordillera far south in Bolivia; Barnes et al., 2008; Henry & Pollack, 1988), and up-to-30 km
712 crustal seismicity respectively (Figure 3a). Thus, the Abancay Deflection cannot be defined
713 as a tectonic aneurism.

714 The similarity in structural and geomorphic setting between the Abancay Deflection
715 and the Himalayan/Alaskan syntaxes, leads us to speculate that the Abancay Deflection may
716 reflect an incipient Andean syntaxis, where drainage capture and ensuing rapid incision of the
717 plateau edge led to focused exhumation and tectonic uplift along a deflected fault pattern. In
718 such a geodynamic context, associated to ocean – continent convergence, the closest

719 comparison can be done with the Denali syntaxis in Alaska (Figure 14). The Abancay
720 Deflection, however, do not reach yet (and maybe never) a mature stage of a tectonic
721 aneurism.

722 **Table 4**. Compilation of observations and comparison of documented tectonic syntaxes with the Abancay Deflection

Observation	Himalayan syntaxis	Alaskan syntaxis	Abancay Deflection
Morphology			
Positive anomaly of topography	**YES** Nanga Parbat mountains (NP) Namche Barwa mountains (NB) (Zeitler et al., 2001)	**YES** Denali mountains St Elias mount (Enkelmann et al., 2017)	**YES** Cordillera Vilcabamba (Salcantay, southern Eastern Cordillera) (Gérard et al. submitted)
High relief and incision	**YES** Indus River (NP) / Tsangpo River (NB) (Zeitler et al., 2001)	**YES** Seward et Logan glaciers (Enkelmann et al., 2017)	**YES** Urubamba River (Gérard et al. submitted)
Major crossing-orogens rivers	**YES** Indus River (NP) / Tsangpo River (NB) (Zeitler et al., 2001)	**NA*** Glaciated area	**YES** Urubamba River (This study; Gérard et al. submitted)
Captured high elevation plateau upstream	**YES** Tibetan plateau (Clark et al., 2004; Yang et al., 2016)	**NO** No plateau	**YES** Altiplano (This study; Gérard et al. submitted)

Observation	Himalayan syntaxis	Alaskan syntaxis	Abancay Deflection
Tightened and aligned rivers along active faults	**YES** Salween, Mekong / Yangtze Rivers (NB; Hallet & Molnar, 2001); Hari, Murgab et Helmand Rivers (NP; Brookfield, 1998)	**NA*** Glaciated area	**YES** Urubamba and Apurimac Rivers along the Apurimac fault system (This study; Gérard et al. submitted)
Knickpoints	**YES** Tsangpo River crossing the NB (Zeitler et al., 2001)	**NA*** Masked bedrock beneath the glaciers	**YES** Urubamba River crossing the Eastern Cordillera (Gérard et al. submitted)
<u>Tectonics and Geodynamic</u>			
Tectonic rotation and strike-slip faulting	**YES** Crustal folding through orogen-parallel compression (Royden et al., 1997) Jiali-Parlung fault (NB; Burg et al., 1998) Karakorum fault (NP; Bossart et al., 1988)	**YES** Fairweather fault (Chapman et al., 2012)	**YES** Counterclockwise rotation and left-lateral component of the Apurimac fault during Miocene (Dalmayrac et al., 1980; Roperch et al., 2006)
Thick-skinned tectonic	**YES** (Zeitler et al., 2001)	**YES** (Chapman et al., 2012)	**YES** Apurimac fault delimiting 2 crustal blocks (This study; Carlier et al., 2005)

Observation	Himalayan syntaxis	Alaskan syntaxis	Abancay Deflection
Localized deformation along crustal-scale faults and magmatic fluid circulation	**YES** (NP; Edwards et al., 2000; Schneider et al., 1999; Seeber & Pêcher, 1998)	**YES** Except for fluids circulation (Koons et al., 2010, 2013)	**YES** Apurimac fault and volcanic fluids circulation since ~7 Ma (Carlier et al., 1996; Carlier et al., 2005)
Indenter	**YES** Indian plate (Burtman & Molnar, 1993)	**YES** Yakutat terrane (Koons et al., 2010; Marechal et al., 2015)	**YES** Arequipa terrane (Ramos, 2010; Villegas-Lanza et al., 2016)
Higher exhumation rates into the core of the syntaxis	**YES** ~10 km/m.y. since ~1 Ma (King et al., 2016)	**YES** ~2 to ~5 km/m.y. since ~2 Ma (Enkelmann et al., 2009; Enkelmann et al., 2017; Falkowski et al., 2014)	**YES** ~1,2 km/m.y. since ~5 Ma (This study)
Conclusion			
Tectonic syntaxis	**YES**	**YES**	**YES**

*Not applicable

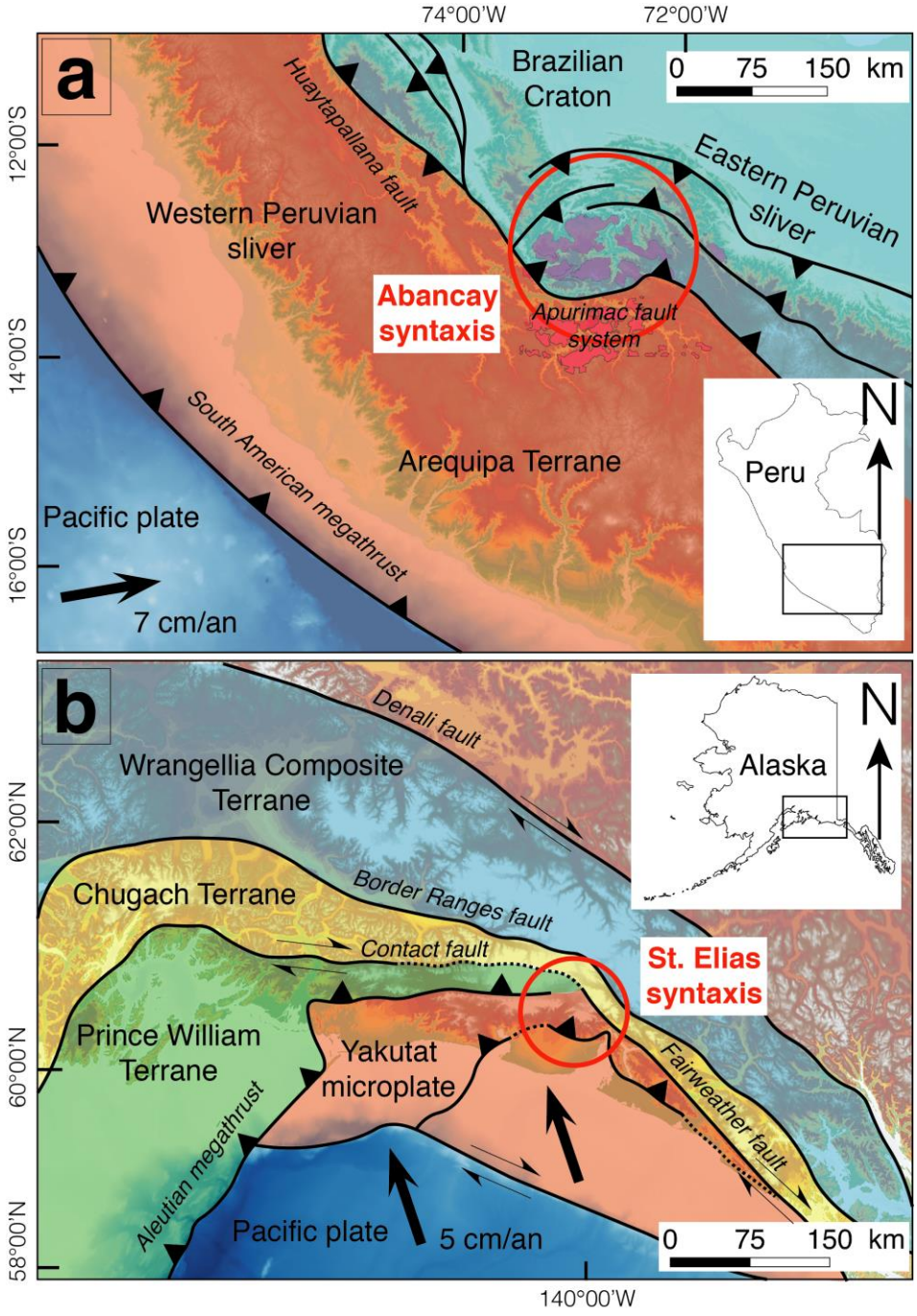

Figure 14. Geodynamic comparison between the Abancay Deflection and the St Elias syntaxis of Alaska. a) The Abancay Deflection case; the bulls-eye structure and morphology of the Abancay Deflection (red circle) suggests that it is an incipient syntaxis, with the Arequipa terrane acting as the indenter. b) The St Elias case from Falkowski et al. (2014). The Yakutat microplate plays the role of the indenter for this Alaskan syntaxis.

6 Conclusions

Our new thermochronological data and inverse thermo(-kinematic) modeling from the Abancay Deflection reveal steady and spatially-uniform exhumation for the whole study area between 40 and 5 Ma, at a moderate rate of ~0.2 km/m.y. We interpret the exhumation rate as evidence for large-scale crustal shortening and/or lower crustal flow associated to low-magnitude erosion rates in an internally-drained area. The differential exhumation of the Abancay Deflection area initiated at ~5 Ma, characterized by ~500% increase in exhumation rate for the southern Eastern Cordillera (~1.2 km/m.y). This 5-Ma exhumation signal has been driven by incision (capture of the paleo-endoreic environment) and enhanced by tectonically driven rock uplift through the Apurimac fault system activation as a south-verging backthrust. For the first time, we document the recent (< 5 Ma) and ongoing tectonic activity of this fault system. Finally, we propose the late-Miocene precipitation intensification and the Arequipa terrane underplating as potential triggers for the re-activation of this out-of-sequence inherited crustal-scale thrust. Considering such a geomorphic and structural setting together with rapid and focused exhumation, in a region of anomalously high relief and topography, we speculate that the Abancay Deflection may represent the first identified incipient Andean syntaxis.

Acknowledgements

This work was supported by the IRD (Institut de Recherche pour le Développement), ISTerre, the INSU (Institut National des Sciences de l'Univers), and the ANR-12-NS06-0005-01 project for the AHe analysis. We are grateful to the SERNANP, the INGEMMET (Cusco-PATA convenio 006-2016-Fondecyt) and the National Archaeological Park of Machu Picchu, for the provided facilities. We thank P.H. Leloup and G. Mahéo (Géode laboratory, Lyon) and the GTC platform (F. Coeur & F. Sénebier, ISTerre, Grenoble) for sample

processing, as well as M. Balvay, R. Pinna-Jamme & F. Haurine for assistance during AFT and AHe dating. Datasets for this research are included in this paper (and its supplementary information files).

References

Allmendinger, R. W., Smalley, R., Bevis, M., Caprio, H., & Brooks, B. (2005). Bending the Bolivian orocline in real time. *Geology*, *33*(11), 905–908. https://doi.org/10.1130/G21779.1

Anderson, R. B., Long, S. P., Horton, B. K., Thomson, S. N., Calle, A. Z., & Stockli, D. F. (2018). Orogenic Wedge Evolution of the Central Andes, Bolivia (21°S): Implications for Cordilleran Cyclicity. *Tectonics*, *37*(10), 3577–3609. https://doi.org/10.1029/2018TC005132

Armijo, R., Lacassin, R., Coudurier-Curveur, A., & Carrizo, D. (2015). Coupled tectonic evolution of Andean orogeny and global climate. *Earth-Science Reviews*. Elsevier B.V. https://doi.org/10.1016/j.earscirev.2015.01.005

Arndt, J., Bartel, T., Scheuber, E., & Schilling, F. (1997). Thermal and rheological properties of granodioritic rocks from the Central Andes, North Chile. *Tectonophysics*, *271*(1–2), 75–88. https://doi.org/10.1016/S0040-1951(96)00218-1

Ault, A. K., Gautheron, C., & King, G. E. (2019). Innovations in (U-Th)/He, fission-track, and trapped-charge thermochronometry with applications to earthquakes, weathering, surface-mantle connections, and the growth and decay of mountains. *Tectonics*. https://doi.org/10.1029/2018tc005312

Barnes, J B, & Ehlers, T. A. (2009). End member models for Andean Plateau uplift. *Earth-Science Reviews*. Elsevier B.V. https://doi.org/10.1016/j.earscirev.2009.08.003

Barnes, Jason B., Ehlers, T. A., Insel, N., McQuarrie, N., & Poulsen, C. J. (2012). Linking

orography, climate, and exhumation across the central Andes. *Geology*, *40*(12), 1135–1138. https://doi.org/10.1130/G33229.1

Barnes, Jason B, Ehlers, T. A., McQuarrie, N., O'Sullivan, P. B., & Tawackoli, S. (2008). Thermochronometer record of central Andean Plateau growth, Bolivia (19.5°S). *Tectonics*, *27*(3). https://doi.org/10.1029/2007TC002174

Bonhomme, M., Fornari, M., Laubacher, G., Sébrier, M., & Vivier, G. (1988). New Cenozoic K-Ar ages on volcanic rocks from the eastern High Andes, southern Peru. *Journal of South American Earth Sciences*, *1*(2), 179–183.

Bossart, P., Dietrich, D., Greco, A., Ottiger, R., & Ramsay, J. (1988). The Tectonic Structure of the Hazara-Kashmir Syntaxis, Southern Himalayas, Pakistan. *Tectonics*, *7*(2), 273–297.

Braun, J. (2003). Pecube: A new finite-element code to solve the 3D heat transport equation including the effects of a time-varying, finite amplitude surface topography. *Computers and Geosciences*, *29*(6), 787–794. https://doi.org/10.1016/S0098-3004(03)00052-9

Braun, J., van der Beek, P., Valla, P., Robert, X., Herman, F., Glotzbach, C., et al. (2012). Quantifying rates of landscape evolution and tectonic processes by thermochronology and numerical modeling of crustal heat transport using PECUBE. *Tectonophysics*, *524–525*, 1–28. https://doi.org/10.1016/j.tecto.2011.12.035

Brookfield, M. E. (1998). The evolution of the great river systems of southern Asia during the Cenozoic India-Asia collision: rivers draining southwards. *Geomorphology*, *22*(3–4), 285–312. https://doi.org/10.1016/S0169-555X(97)00082-2

Brown, R. W., Beucher, R., Roper, S., Persano, C., Stuart, F., & Fitzgerald, P. (2013). Natural age dispersion arising from the analysis of broken crystals. Part I: Theoretical basis and implications for the apatite (U-Th)/He thermochronometer. *Geochimica et Cosmochimica Acta*, *122*(120), 478–497. https://doi.org/10.1016/j.gca.2013.05.041

807 Burg, J. P., Nievergelt, P., Oberli, F., Seward, D., Davy, P., Maurin, J. C., et al. (1998). The
808 Namche Barwa syntaxis: Evidence for exhumation related to compressional crustal
809 folding. *Journal of Asian Earth Sciences*, *16*(2–3), 239–252.
810 https://doi.org/10.1016/S0743-9547(98)00002-6
811 Burtman, V., & Molnar, P. (1993). Geological and geophysical evidence for deep subduction
812 of continental crust beneath the Pamir. *Geological Society of America Special Paper*,
813 *281*, 1–76.
814 Cabrera, J., Sébrier, M., & Mercier, J. L. (1991). Plio-Quaternary geodynamic evolution of a
815 segment of the Peruvian Andean Cordillera located above the change in the subduction
816 geometry: the Cuzco region. *Tectonophysics*, *190*(2–4), 331–362.
817 https://doi.org/10.1016/0040-1951(91)90437-W
818 Carlier, G, Lorand, J. P., Bonhomme, M., & Carlotto, V. (1996). A reappraisal of the
819 cenozoic inner arc magmatism in southern Peru: consequences for the evolution of the
820 central Andes for the past 50 Ma. *Third ISAG*, (January), 551–554.
821 Carlier, Gabi, Lorand, J. P., Liégeois, J. P., Fornari, M., Soler, P., Carlotto, V., & Cárdenas, J.
822 (2005). Potassic-ultrapotassic mafic rocks delineate two lithospheric mantle blocks
823 beneath the southern Peruvian Altiplano. *Geology*, *33*(7), 601–604.
824 https://doi.org/10.1130/G21643.1
825 Carlotto, V. (2013). Paleogeographic and tectonic controls on the evolution of Cenozoic
826 basins in the Altiplano and Western Cordillera of southern Peru. *Tectonophysics*, *589*,
827 195–219. https://doi.org/10.1016/j.tecto.2013.01.002
828 Chapman, J. B., Pavlis, T. L., Bruhn, R. L., Worthington, L. L., Gulick, S. P. S., & Berger, A.
829 L. (2012). Structural relationships in the eastern syntaxis of the St. Elias orogen, Alaska.
830 *Geosphere*, *8*(1), 105–126. https://doi.org/10.1130/GES00677.1
831 Clark, M. K., Schoenbohm, L. M., Royden, L. H., Whipple, K. X., Burchfiel, B. C., Zhang,

X., et al. (2004). Surface uplift, tectonics, and erosion of eastern Tibet from large-scale drainage patterns. *Tectonics*, *23*(1), 1–21. https://doi.org/10.1029/2002TC001402

Craw, D., Koons, P. O., Winslow, D., Chamberlain, C. P., & Zeitler, P. (1994). Boiling fluids in a region of rapid uplift, Nanga Parbat Massif, Pakistan. *Earth and Planetary Science Letters*, *128*(3–4), 169–182. https://doi.org/10.1016/0012-821X(94)90143-0

Dalmayrac, B., Laubacher, G., & Marocco, R. (1980). *Géologie des Andes péruviennes* (ORSTOM). Paris.

Dorbath, C., Dorbath, L., Cisternas, A., Deverchére, J., & Sebrier, M. (1990). Seismicity of the huancayo basin (central Peru) and the huaytapallana fault. *Journal of South American Earth Sciences*, *3*(1), 21–29. https://doi.org/10.1016/0895-9811(90)90015-S

Dziewonski, A. M., Chou, T. A., & Woodhouse, J. H. (1981). Determination of earthquake source parameters from waveform data for studies of global and regional seismicity. *Journal of Geophysical Research*, *86*(B4), 2825–2852. https://doi.org/10.1029/JB086iB04p02825

Edwards, M. A., Kidd, W. S. F., Khan, M. A., & Schneider, D. A. (2000). Tectonics of the SW margin of the Nanga Parbat-Haramosh massif. *Geological Society, London, Special Publications*, (170), 77–100.

Egeler, C., & De Booy, T. (1961). Preliminary Note on the Geology of the Cordillera Vilcabamba (SE Peru), with Emphasis on the... *Geologie & Mijnbouw*, *40*(3), 319–325.

Ehlers, T. A., Chaudhri, T., Kumar, S., Fuller, C. W., Willett, S. D., Ketcham, R. A., & Brandon, M. T. (2005). Computational Tools for Low-Temperature Thermochronometer Interpretation. *Reviews in Mineralogy and Geochemistry*, *58*(1), 589–622. https://doi.org/10.2138/rmg.2005.58.22

Ehlers, Todd A, & Poulsen, C. J. (2009). Influence of Andean uplift on climate and paleoaltimetry estimates. *Earth and Planetary Science Letters*, *281*(3–4), 238–248.

https://doi.org/10.1016/j.epsl.2009.02.026

Ekström, G., Nettles, M., & Dziewoński, A. M. (2012). The global CMT project 2004-2010: Centroid-moment tensors for 13,017 earthquakes. *Physics of the Earth and Planetary Interiors*, *200–201*, 1–9. https://doi.org/10.1016/j.pepi.2012.04.002

Enkelmann, E., Zeitler, P. K., Pavlis, T. L., Garver, J. I., & Ridgway, K. D. (2009). Intense localized rock uplift and erosion in the StElias orogen of Alaska. *Nature Geoscience*, *2*(5), 360–363. https://doi.org/10.1038/ngeo502

Enkelmann, Eva, Piestrzeniewicz, A., Falkowski, S., Stübner, K., & Ehlers, T. A. (2017). Thermochronology in southeast Alaska and southwest Yukon: Implications for North American Plate response to terrane accretion. *Earth and Planetary Science Letters*, *457*, 348–358. https://doi.org/10.1016/j.epsl.2016.10.032

Espurt, N., Barbarand, J., Roddaz, M., Brusset, S., Baby, P., Saillard, M., & Hermoza, W. (2011). A scenario for late Neogene Andean shortening transfer in the Camisea Subandean zone (Peru, 12°S): Implications for growth of the northern Andean Plateau. *Bulletin of the Geological Society of America*, *123*(9–10), 2050–2068. https://doi.org/10.1130/B30165.1

Evans, N. J., Byrne, J. P., Keegan, J. T., & Dotter, L. E. (2005). Determination of Uranium and Thorium in Zircon, Apatite, and Fluorite: Application to Laser (U–Th)/He Thermochronology. *Journal of Analytical Chemistry*, *60*(12), 1159–1165.

Falkowski, S., Enkelmann, E., & Ehlers, T. A. (2014). Constraining the area of rapid and deep-seated exhumation at the St. Elias syntaxis, Southeast Alaska, with detrital zircon fission-track analysis. *Tectonics*, *33*(5), 597–616. https://doi.org/10.1002/2013TC003408

Farley, K A. (2000). Helium diffusion from apatite: General behavior as illustrated by Durango fluorapatite. *Journal of Geophysical Research: Solid Earth*, *105*(B2), 2903–

2914. https://doi.org/10.1029/1999jb900348

Farley, Kenneth A. (2002). (U-Th)/He Dating: Techniques, Calibrations, and Applications. *Reviews in Mineralogy and Geochemistry*, *47*, 819–844. https://doi.org/10.2138/rmg.2002.47.18

Galbraith, R. F., & Laslett, G. M. (1993). Statistical models for mixed fission track ages. *International Journal of Radiation Applications and Instrumentation. Part*, *21*(4), 459–470. https://doi.org/10.1016/1359-0189(93)90185-C

Gallagher, K. (2012). Transdimensional inverse thermal history modeling for quantitative thermochronology. *Journal of Geophysical Research: Solid Earth*, *117*(2), 1–16. https://doi.org/10.1029/2011JB008825

Garzione, C. N., Molnar, P., Libarkin, J. C., & MacFadden, B. J. (2006). Rapid late Miocene rise of the Bolivian Altiplano: Evidence for removal of mantle lithosphere. *Earth and Planetary Science Letters*, *241*(3–4), 543–556. https://doi.org/10.1016/j.epsl.2005.11.026

Garzione, C. N., McQuarrie, N., Perez, N. D., Ehlers, T. A., Beck, S. L., Kar, N., et al. (2017). Tectonic Evolution of the Central Andean Plateau and Implications for the Growth of Plateaus. *Annual Review of Earth and Planetary Sciences*, *45*(1), 529–559. https://doi.org/10.1146/annurev-earth-063016-020612

Gautheron, C., & Tassan-Got, L. (2010). A Monte Carlo approach to diffusion applied to noble gas/helium thermochronology. *Chemical Geology*, *273*(3–4), 212–224. https://doi.org/10.1016/j.chemgeo.2010.02.023

Gautheron, C., Tassan-Got, L., Barbarand, J., & Pagel, M. (2009). Effect of alpha-damage annealing on apatite (U-Th)/He thermochronology. *Chemical Geology*, *266*(3–4), 166–179. https://doi.org/10.1016/j.chemgeo.2009.06.001

Gautheron, C., Tassan-Got, L., Ketcham, R. A., & Dobson, K. J. (2012). Accounting for long

907 alpha-particle stopping distances in (U-Th-Sm)/He geochronology: 3D modeling of
908 diffusion, zoning, implantation, and abrasion. *Geochimica et Cosmochimica Acta*, *96*,
909 44–56. https://doi.org/10.1016/j.gca.2012.08.016
910 Gautheron, C., Espurt, N., Barbarand, J., Roddaz, M., Baby, P., Brusset, S., et al. (2013).
911 Direct dating of thick- and thin-skin thrusts in the Peruvian Subandean zone through
912 apatite (U-Th)/He and fission track thermochronometry. *Basin Research*, *25*(4), 419–
913 435. https://doi.org/10.1111/bre.12012
914 Glotzbach, C., van der Beek, P. A., & Spiegel, C. (2011). Episodic exhumation and relief
915 growth in the Mont Blanc massif, Western Alps from numerical modelling of
916 thermochronology data. *Earth and Planetary Science Letters*, *304*(3–4), 417–430.
917 https://doi.org/10.1016/j.epsl.2011.02.020
918 Gonfiantini, R., Roche, M.-A., Olivry, J.-C., Fontes, J.-C., & Zuppi, G. M. (2001). The
919 altitude effect on the isotopic composition of tropical rains. *Chemical Geology*, (181),
920 147–167.
921 Gotberg, N., McQuarrie, N., & Caillaux, V. C. (2010). Comparison of crustal thickening
922 budget and shortening estimates in southern Peru (12 14°S): Implications for mass
923 balance and rotations in the "Bolivian orocline." *Bulletin of the Geological Society of*
924 *America*, *122*(5–6), 727–742. https://doi.org/10.1130/B26477.1
925 Green, P. F. (1981). A new look at statistics in fission-track dating. *Nuclear Tracks*, *5*, 77–86.
926 Hallet, B., & Molnar, P. (2001). Distorted drainage basins as markers of crustal strain east of
927 the Himalaya. *Journal of Geophysical Research: Solid Earth*, *106*(B7), 13697–13709.
928 https://doi.org/10.1029/2000jb900335
929 Henry, S., & Pollack, H. (1988). Terrestrial Heat Flow Above the Andean Subduction Zone
930 in Bolivia and Peru. *Journal of Geophysical Research*, *93*(B12), 153–162.
931 https://doi.org/10.1029/JB093iB12p15153

Horton, B. K. (2005). Revised deformation history of the central Andes: Inferences from Cenozoic foredeep and intermontane basins of the Eastern Cordillera, Bolivia. *Tectonics*. https://doi.org/10.1029/2003TC001619

Horton, B. K., Perez, N. D., Fitch, J. D., & Saylor, J. E. (2014). Punctuated shortening and subsidence in the Altiplano Plateau of southern Peru: Implications for early Andean mountain building. *Lithosphere*, *7*(2), 117–137. https://doi.org/10.1130/L397.1

Husson, L., & Sempere, T. (2003). Thickening the Altiplano crust by gravity-driven crustal channel flow. *Geophysical Research Letters*, *30*(5), 1–4. https://doi.org/10.1029/2002GL016877

Insel, N., Poulsen, C. J., & Ehlers, T. A. (2010). Influence of the Andes Mountains on South American moisture transport, convection, and precipitation. *Climate Dynamics*, *35*(7), 1477–1492. https://doi.org/10.1007/s00382-009-0637-1

Jaillard, E., & Soler, P. (1996). Cretaceous to early Paleogene tectonic evolution of the northern Central Andes (0-18 degrees S) and its relations to geodynamics. *Tectonophysics*, *259*(2), 41–53. https://doi.org/10.1016/0040-1951(95)00107-7

Kar, N., Garzione, C. N., Jaramillo, C., Shanahan, T., Carlotto, V., Pullen, A., et al. (2016). Rapid regional surface uplift of the northern Altiplano plateau revealed by multiproxy paleoclimate reconstruction. *Earth and Planetary Science Letters*, *447*, 33–47. https://doi.org/10.1016/j.epsl.2016.04.025

Kennan, L. (2008). Fission track ages and sedimentary provenance studies in Peru, and their implications for andean paleogeographic evolution, stratigraphy and hydrocarbon systems. *VI INGEPET*. Retrieved from http://www.agu.org/pubs/crossref/1988/JB093iB12p15153.shtml

Ketcham, R. A., Donelick, R. A., & Carlson, W. D. (1999). Variability of apatite fission-track annealing kinetics: III. Crystallographic orientation effects. *American*

Mineralogist, *84*, 1235–1255. https://doi.org/10.2138/am-1999-0902

Ketcham, R. A., Carter, A., Donelick, R. A., Barbarand, J., & Hurford, A. J. (2007). Improved modeling of fission-track annealing in apatite. *American Mineralogist*, *92*(5–6), 799–810. https://doi.org/10.2138/am.2007.2281

Ketcham, R. A., Gautheron, C., & Tassan-Got, L. (2011). Accounting for long alpha-particle stopping distances in (U-Th-Sm)/He geochronology: Refinement of the baseline case. *Geochimica et Cosmochimica Acta*, *75*(24), 7779–7791. https://doi.org/10.1016/j.gca.2011.10.011

King, G. E., Herman, F., & Guralnik, B. (2016). Northward migration of the eastern Himalayan syntaxis revealed by OSL thermochronometry. *Science*, *353*(6301), 800–804. https://doi.org/10.1126/science.aaf2637

Koons, P. O., Hooks, B. P., Pavlis, T., Upton, P., & Barker, A. D. (2010). Three-dimensional mechanics of Yakutat convergence in the southern Alaskan plate corner. *Tectonics*, *29*(4), 1–17. https://doi.org/10.1029/2009TC002463

Koons, P. O., Zeitler, P. K., & Hallet, B. (2013). Tectonic Aneurysms and Mountain Building. In *Treatise on Geomorphology* (Vol. 5, pp. 318–349). https://doi.org/10.1016/B978-0-12-374739-6.00094-4

Lamb, S. (2011). Did shortening in thick crust cause rapid Late Cenozoic uplift in the northern Bolivian Andes? *Journal of the Geological Society*, *168*(5), 1079–1092. https://doi.org/10.1144/0016-76492011-008

Lancelot, J. R., Laubacher, G., Marocco, R., & Renaud, U. (1978). U/Pb radiochronology of two granitic plutons from the eastern Cordillera (Peru) - Extent of Permian magmatic activity and consequences. *Geologische Rundschau*, *67*(1), 236–243. https://doi.org/10.1007/BF01803263

Lease, R. O., & Ehlers, T. A. (2013). Incision into the eastern Andean Plateau during

Pliocene cooling. *Science*, *341*(6147), 774–776. https://doi.org/10.1126/science.1239132

Loewy, S. L., Connelly, J. N., & Dalziel, I. W. D. (2004). An orphaned basement block: The Arequipa-Antofalla Basement of the central Andean margin of South America. *Bulletin of the Geological Society of America*, *116*(1–2), 171–187. https://doi.org/10.1130/B25226.1

Mamani, M., Wörner, G., & Sempere, T. (2010). Geochemical variations in igneous rocks of the Central Andean orocline (13°S to 18°S): Tracing crustal thickening and magma generation through time and space. *Bulletin of the Geological Society of America*, *122*(1–2), 162–182. https://doi.org/10.1130/B26538.1

Marechal, A., Mazzotti, S., Elliott, J., Freymueller, J., & Schmidt, M. (2015). Indentor-corner tectonics in the Yakutat-St. Elias collision constrained by GPS. *Journal of Geophysical Research: Solid Earth*, *120*, 3897–3908. https://doi.org/10.1002/2015JB012608.Received

Marocco, R. (1971). Etude géologique de la chaîne andine au niveau de la déflexion d'Abancay (Pérou). *Cah. ORSTOM*, (1971), 45–58.

Meltzer, A. S., Sarker, G. L., Seeber, L., & Armbruster, J. (1998). Snap, crackel, pop! Seismicity and crustal structure at Nanga Parbat, Pakistan, Himalaya. *Eos (Transactions, American Geophysical Union*, *79*(F909).

Mercier, L., Sébrier, M., Lavenu, A., Cabrera, J., Bellier, O., Dumont, J. ., & Machare, J. (1992). Changes in the Tectonic Regime Above a Subduction Zone of Andean Type: The Andes of Peru and Bolivia During the Pliocene-Pleistocene. *Journal of Geophysical Research*, *97*(B8), 945–982.

Mišković, A., Spikings, R. A., Chew, D. M., Košler, J., Ulianov, A., & Schaltegger, U. (2009). Tectonomagmatic evolution of Western Amazonia: Geochemical characterization and zircon U-Pb geochronologic constraints from the Peruvian Eastern

Cordilleran granitoids. *Bulletin of the Geological Society of America*, *121*(9–10), 1298–1324. https://doi.org/10.1130/B26488.1

Mosolf, J. G., Horton, B. K., Heizler, M. T., & Matos, R. (2011). Unroofing the core of the central Andean fold-thrust belt during focused late Miocene exhumation: Evidence from the Tipuani-Mapiri wedge-top basin, Bolivia. *Basin Research*, *23*(3), 346–360. https://doi.org/10.1111/j.1365-2117.2010.00491.x

Müller, J. P., Kley, J., & Jacobshagen, V. (2002). Structure and Cenozoic kinematics of the Eastern Cordillera, southern Bolivia (21°S). *Tectonics*, *21*(5), 1-1-1–24. https://doi.org/10.1029/2001tc001340

Norton, K., & Schlunegger, F. (2011). Migrating deformation in the Central Andes from enhanced orographic rainfall. *Nature Communications*, *2*(1). https://doi.org/10.1038/ncomms1590

Ouimet, W. B., & Cook, K. L. (2010). Building the central Andes through axial lower crustal flow. *Tectonics*, *29*(3), 1–15. https://doi.org/10.1029/2009TC002460

Peizhen, Z., Molnar, P., & Downs, W. R. (2001). Increased sedimentation rates and grain sizes 2-4 Ma ago due to the influence of climate change on erosion rates. *Nature*, *410*(April), 891–897. https://doi.org/http://www.nature.com/nature/journal/v410/n6831/suppinfo/410891a0_S1.html

Perello, J., Carlotto, V., Zarate, A., Ramos, P., Posso, H., Neyra, C., et al. (2003). Porphyry-Style Alteration and Mineralization of the Middle Eocene to Early Oligocene Andahuaylas-Yauri Belt , Cuzco Region , Peru. *Economic Geology*, *98*, 1575–1605.

Perez, N. D., Horton, B. K., & Carlotto, V. (2016). Structural inheritance and selective reactivation in the central Andes: Cenozoic deformation guided by pre-Andean structures in southern Peru. *Tectonophysics*, *671*, 264–280.

https://doi.org/10.1016/j.tecto.2015.12.031

Phillips, K., Clayton, R. W., Davis, P., Tavera, H., Guy, R., Skinner, S., et al. (2012). Structure of the subduction system in southern Peru from seismic array data. *Journal of Geophysical Research*, *117*(11), 1–17. https://doi.org/10.1029/2012JB009540

Poulsen, C. J., Ehlers, T. A., & Insel, N. (2010). Onset of Convective Rainfall During Gradual Late Miocene Rise of the Central Andes. *Science*, *328*(April), 490–494. https://doi.org/10.1126/science.1185078

Rak, A. J., McQuarrie, N., & Ehlers, T. A. (2017). Kinematics, Exhumation, and Sedimentation of the North Central Andes (Bolivia): An Integrated Thermochronometer and Thermokinematic Modeling Approach. *Tectonics*, *36*(11), 2524–2554. https://doi.org/10.1002/2016TC004440

Ramos, V. A. (2008). The Basement of the Central Andes: The Arequipa and Related Terranes. *Annual Review of Earth and Planetary Sciences*, *36*(1), 289–324. https://doi.org/10.1146/annurev.earth.36.031207.124304

Ramos, V. A. (2010). The Grenville-age basement of the Andes. *Journal of South American Earth Sciences*, *29*(1), 77–91. https://doi.org/10.1016/j.jsames.2009.09.004

Recanati, A., Gautheron, C., Barbarand, J., Missenard, Y., Pinna-Jamme, R., Tassan-Got, L., et al. (2017). Helium trapping in apatite damage: Insights from (U-Th-Sm)/He dating of different granitoid lithologies. *Chemical Geology*, *470*(September), 116–131. https://doi.org/10.1016/j.chemgeo.2017.09.002

Reiners, P. W., & Brandon, M. T. (2006). Using Thermochronology To Understand Orogenic Erosion. *Annual Review of Earth and Planetary Sciences*, *34*(1), 419–466. https://doi.org/10.1146/annurev.earth.34.031405.125202

Reiners, P. W., & Shuster, D. L. (2009). Thermochronology and landscape evolution. *Physics Today*, (September), 31–36.

Reitsma, M. J. (2012). *Reconstructing the Late Paleozoic - Early Mesozoic plutonic and sedimentary record of south-east Peru : Orphaned back-arcs along the western margin of Gondwana*.

Robert, X., Van Der Beek, P., Braun, J., Perry, C., & Mugnier, J. L. (2011). Control of detachment geometry on lateral variations in exhumation rates in the Himalaya: Insights from low-temperature thermochronology and numerical modeling. *Journal of Geophysical Research: Solid Earth*, *116*(5), 1–22. https://doi.org/10.1029/2010JB007893

Roperch, P., Sempere, T., Macedo, O., Arriagada, C., Fornari, M., Tapia, C., et al. (2006). Counterclockwise rotation of late Eocene-Oligocene fore-arc deposits in southern Peru and its significance for oroclinal bending in the central Andes. *Tectonics*, *25*(3). https://doi.org/10.1029/2005TC001882

Royden, L. H., Burchfiel, B. C., King, R. W., Wang, E., Chen, Z., Shen, F., & Liu, Y. (1997). Surface deformation and lower crustal flow in eastern Tibet. *Science*, *276*(5313), 788–790. https://doi.org/10.1126/science.276.5313.788

Ruiz, G. M. H., Carlotto, V., Van Heiningen, P. V., & Andriessen, P. A. M. (2009). Steady-state exhumation pattern in the Central Andes – SE Peru. *Geological Society, London, Special Publications*, *324*(1), 307–316. https://doi.org/10.1144/SP324.20

Sambridge, M. (1999). Geophysical inversion with a neighbourhood algorithm –II. Appraising the ensemble. *Geophys. J. Int.*, *138*, 727–746.

Sambridge, Malcolm. (1999). Geophysical inversion with a neighbourhood algorithm - I. Searching a parameter space. *Geophysical Journal International*, *138*(2), 479–494. https://doi.org/10.1046/j.1365-246X.1999.00876.x

Schneider, D. A., Edwards, M. A., Kidd, W. S. F., Asif Khan, M., Seeber, L., & Zeitler, P. K. (1999). Tectonics of Nanga Parbat, western Himalaya: Synkinematic plutonism within

1082 the doubly vergent shear zones of a crustal-scale pop-up structure. *Geology*, *27*(11),
1083 999–1002. https://doi.org/10.1130/0091-7613(1999)027<0999:TONPWH>2.3.CO;2
1084 Schwarz, G. E. (1978). Estimating the dimension of a model. *Annu. Stat.*, *6*, 461–464.
1085 Sébrier, M., Mercier, L., Francois, M., Laubacher, G., & Carey-Gailhardis, E. (1985).
1086 Quaternary Normal and Reverse Faulting and the State of Stress in the Central Andes of
1087 South Peru. *Tectonics*, *4*(7), 739–780.
1088 Seeber, L., & Pêcher, A. (1998). Strain partitioning along the Himalayan arc and the Nanga
1089 Parbat antiform. *Geology*, *26*(9), 791–794. https://doi.org/10.1130/0091-
1090 7613(1998)026<0791:SPATHA>2.3.CO;2
1091 Sempere, T., Carlier, G., Soler, P., Fornari, M., Carlotto, V., Jacay, J., et al. (2002). Late
1092 Permian-Middle Jurassic lithospheric thinning in Peru and Bolivia, and its bearing on
1093 Andean-age tectonics. *Tectonophysics*, *345*(1–4), 153–181.
1094 https://doi.org/10.1016/S0040-1951(01)00211-6
1095 Shuster, D. L., Flowers, R. M., & Farley, K. A. (2006). The influence of natural radiation
1096 damage on helium diffusion kinetics in apatite. *Earth and Planetary Science Letters*,
1097 *249*(3–4), 148–161. https://doi.org/10.1016/j.epsl.2006.07.028
1098 Sobolev, S. V., & Babeyko, A. Y. (2005). What drives orogeny in the Andes? *Geology*,
1099 *33*(8), 617–620. https://doi.org/10.1130/G21557.1
1100 Springer, M. (1999). Interpretation of heat-flow density in the Central Andes. In
1101 *Tectonophysics* (Vol. 306, pp. 377–395). https://doi.org/10.1016/S0040-1951(99)00067-
1102 0
1103 Strecker, M. R., Alonso, R. N., Bookhagen, B., Carrapa, B., Hilley, G. E., Sobel, E. R., &
1104 Trauth, M. H. (2007). Tectonics and Climate of the Southern Central Andes. *Annual*
1105 *Review of Earth and Planetary Sciences*, *35*(1), 747–787.
1106 https://doi.org/10.1146/annurev.earth.35.031306.140158

Stüwe, K., White, L., & Brown, R. (1994). The influence of eroding topography on steady-state isotherms. Application to fission track analysis. *Earth and Planetary Science Letters*, *124*, 63–74.

Suarez, G., Molnar, P., & Burchfiel, B. C. (1983). Seismicity, fault plane solutions, depth of faulting, and active tectonics of the Andes of Peru, Ecuador, and southern Colombia. *Journal of Geophysical Research*, *88*(B12), 10403–10428. https://doi.org/10.1029/JB088iB12p10403

Sundell, K. E., Saylor, J. E., Lapen, T. J., & Horton, B. K. (2019). Implications of variable late Cenozoic surface uplift across the Peruvian central Andes. *Scientific Reports*, *9*(1), 1–12. https://doi.org/10.1038/s41598-019-41257-3

Tassara, A. (2005). Interaction between the Nazca and South American plates and formation of the Altiplano-Puna plateau: Review of a flexural analysis along the Andean margin (15°-34°S). *Tectonophysics*, *399*(1-4 SPEC. ISS.), 39–57. https://doi.org/10.1016/j.tecto.2004.12.014

Valla, P. G., Van Der Beek, P. A., Shuster, D. L., Braun, J., Herman, F., Tassan-Got, L., & Gautheron, C. (2012). Late Neogene exhumation and relief development of the Aar and Aiguilles Rouges massifs (Swiss Alps) from low-temperature thermochronology modeling and 4He/3He thermochronometry. *Journal of Geophysical Research: Earth Surface*, *117*(1), 1–23. https://doi.org/10.1029/2011JF002043

Villegas-Lanza, J., Chlieh, M., Cavalié, O., Tavera, H., Baby, P., Chire-Chira, J., & Nocquet, J.-M. (2016). Active tectonics of Peru: Heterogeneous interseismic coupling along the Nazca megathrust, rigid motion of the Peruvian Sliver, and Subandean shortening accommodation. *Journal of Geophysical Research: Solid Earth*, *121*, 7371–7394. https://doi.org/10.1002/2015JB012608.Received

Whipple, K. X., & Meade, B. J. (2004). Controls on the strength of coupling among climate,

erosion, and deformation in two-sided, frictional orogenic wedges at steady state. *Journal of Geophysical Research: Earth Surface*, *109*(F1), 1–24. https://doi.org/10.1029/2003jf000019

Whittington, A. G., Hofmeister, A. M., & Nabelek, P. I. (2009). Temperature-dependent thermal diffusivity of the Earth's crust and implications for magmatism. *Nature*, *458*(7236), 319–321. https://doi.org/10.1038/nature07818

Willett, S., Beaumont, C., & Fullsack, P. (1993). Mechanical model for the tectonics of doubly vergent compressional orogens. *Geology*, *21*(4), 371–374. https://doi.org/10.1130/0091-7613(1993)021<0371:MMFTTO>2.3.CO;2

Wimpenny, S., Copley, A., Benavente, C., & Aguirre, E. (2018). Extension and Dynamics of the Andes Inferred From the 2016 Parina (Huarichancara) Earthquake. *Journal of Geophysical Research: Solid Earth*, *123*(9), 8198–8228. https://doi.org/10.1029/2018JB015588

Yang, R., Fellin, M. G., Herman, F., Willett, S. D., Wang, W., & Maden, C. (2016). Spatial and temporal pattern of erosion in the Three Rivers Region, southeastern Tibet. *Earth and Planetary Science Letters*, *433*, 10–20. https://doi.org/10.1016/j.epsl.2015.10.032

Zeitler, P. K., Meltzer, A. S., Koons, P. 0., Craw, D., Hallet, B., Chamberlain, C. P., et al. (2001). Erosion, Himalayan Geodynamics, and the Geomorphology of Metamorphism. *GSA Today*, *11*(January), 4–9.